Chemical Engineering Research and Design 220 (2025) 482–499

Contents lists available at ScienceDirect

Chemical Engineering Research and Design

journal homepage: www.elsevier.com/locate/cherd

Engineering triphenyl phosphonium conjugated iron oxide nanoparticles for Oxaliplatin loading: Application in cancer treatment

Masome Moeni [a], Mohamed Edokali [a], Matthew Rogers [b], Oscar Cespedes [b], Roya Abedizadeh [c], Hamid Reza Khorasani [c], Elham Aram [c,d], Hamid Sadeghi-Abandansari [e], Jabbar Gardy [f,g], Davood Sabour [c], Andrew Britton [a], Elizabeth Willneff [h], Milene Volpato [i], Robert Menzel [j], Ali Hassanpour [a,*]

[a] School of Chemical and Process Engineering, University of Leeds, Leeds LS2 9JT, UK
[b] School of Physics and Astronomy, University of Leeds, Leeds LS2 9JT, UK
[c] Division of Cancer Medicine, Department of Stem Cells and Developmental Biology, Cell Science Research Center, Royan Institute for Stem Cell Biology and Technology, ACECR, Babol 47138-18983, Iran
[d] Department of Polymer Engineering, Faculty of Engineering, Golestan University, Gorgan 49188-88369, Iran
[e] Department of Cell Engineering, Cell Science Research Center, Royan Institute for Stem Cell Biology and Technology, ACECR, Tehran, Iran
[f] Cormica Bradford Limited, Campus Road, Listerhills Science Park, Bradford BD7 1HR, UK
[g] Chemistry Department, College of Science, Salahaddin University-Erbil, Erbil, Iraqi Kurdistan Region 44002, Iraq
[h] School of Design, University of Leeds, Leeds LS2 9JT, UK
[i] Leeds Institute of Medical Research, St James University Hospital, University of Leeds, Leeds LS9 7TF, UK
[j] School of Chemistry, University of Leeds, Leeds LS2 9JT, UK

ARTICLE INFO

Keywords:
Cancer
Iron oxide nanoparticle
Superparamagnetism
Drug delivery
Drug release
Cell toxicity

ABSTRACT

Cancer remains one of the most pervasive and lethal diseases globally, with conventional chemotherapy often failing to effectively eradicate tumors or prevent their progression (e.g., breast, ovarian, and colon cancers). Iron oxide nanoparticles (Fe_3O_4 NPs) have emerged as promising candidates for drug delivery in cancer treatment due to their excellent biocompatibility, versatile surface chemistry, tunable magnetic properties, and potential for multi-modal applications on a single platform. In this study, the unique contribution lies in the functionalisation of Fe_3O_4 NPs with (3-carboxypropyl) triphenylphosphonium bromide (TPP) and their subsequent loading with the chemotherapeutic agent oxaliplatin (OXA). TPP functionalization can enable mitochondrial targeting, providing a novel strategy to enhance drug delivery efficacy. The Fe_3O_4 NPs were synthesised *via* a co-precipitation reaction at elevated temperature (80 °C) and high pH (11), followed by coating with tetraethyl orthosilicate (TEOS) and 3-aminopropyltriethoxysilane (3-APTES), and functionalisation with TPP. Analytical characterisation (XPS, ICP-OE) confirmed the successful TPP functionalisation and loading of OXA. Notably, the nanoparticles exhibited good stability across a range of temperatures (4 °C, 25 °C, 37 °C, and 43 °C) and retained their superparamagnetic properties, highlighting their suitability for biomedical applications. Cell toxicity analysis has shown that the IC50 values (i.e. the concertation at which 50 % of cell growth is inhibited) of corresponding OXA concentration delivered by the NPs is comparable with the pure OXA, suggesting an effective

Abbreviations: AcB, Acetate buffer; 3-APTES, 3-aminopropyltriethoxysilane; ATR, Attenuated total reflection; BET, Brunauer–Emmett–Teller; D_{BET}, BET particle diameter; CTAB, Cetyltrimethylammonium bromide; D_{311}, Average crystallite size; DAD, Diode array detector; D_H, Hydrodynamic size; DLS, Dynamic light scattering; DMSO, Dimethyl sulfoxide; DOX, Doxorubicin; EDCI, 1-ethyl-3–3-dimethylaminopropyl carbodiimide; EXMF, External magnetic field; FA, Folic acid; FCS, Foetal calf serum; FT-IR, Fourier transfer inferred spectroscopy; FWHM, Full width at half maximum; HAADF, High annular dark-field imaging; HPLCW, HPLC grade water; HR-TEM, High resolution Transmission electron microscopy; ICP-OES, inductively coupled plasma optical emission spectrometer; MRI, Magnetic resonance imaging; MSN, Mesoporous silica nanoparticles; MTT, 3–4,5-dimethylthiazol-2-yl-2,5-dipheynyltetrazolium bromide; NHS, N-hydroxysuccinimide; NMP, N-Methyl-2-pyrrolidone; NPs, Nanoparticles; OXA, Oxaliplatin; PBS, Phosphate buffer solution; PEG, Polyethyleneglycol; PXRD, Powder X-ray diffraction; RCF, relative centrifugal force; RPM, rotational speed per minute; RT, Retention time; S, Section; SAED, Selected area diffraction pattern; SI, Supplementary information; STEP, space and time resolved extinction profiles; T, Tesla; TDD, Targeted drug delivery; TEOS, Tetraethyl orthosilicate; TPP, 3-carboxypropyl triphenyl phosphonium bromide; VSM, Vibrating sample magnetometer; XPS, X-ray photoelectron spectroscopy; UHV, Ultra-high Vacuum; ZP, Zeta potential.

* Corresponding author.
E-mail address: a.hassanpour@leeds.ac.uk (A. Hassanpour).

https://doi.org/10.1016/j.cherd.2025.06.042
Received 2 February 2025; Received in revised form 4 June 2025; Accepted 25 June 2025
Available online 3 July 2025

drug delivery to the cells using NPs. It should be noted that the TPP modification was aimed at enabling mitochondrial targeting and promoting immunogenic cell death, both of which will be further investigated in future *in vitro/in vivo* studies.

1. Introduction

The worldwide burden of cancer remains substantial, and despite advancement in screening and diagnostic strategies, survival rates for many cancers remain relatively low. Among emerging techniques in cancer treatment, the application of magnetic iron oxide nanoparticles (IONPs), in particular Fe_3O_4 nanoparticles (NPs), has gained significant attention in drug delivery. Fe_3O_4 NPs possess numerous advantages properties, such as biocompatibility, tunable surface chemistry and controllable magnetic behaviour, which make them to stand out amongst other inorganic NPs, e.g., gold, and carbon-based NPs (Yang et al., 2020; Sabzi dizajyekan et al., 2024). One of the prominent features of Fe_3O_4 NPs is their magnetic responsiveness, which enables them to be navigated to tumour sites using an External Magnetic Field (EXMF). After releasing their therapeutic payload, they can potentially be retrieved, redirected or removed using the same EXMF. Moreover, due to their incredible biocompatibility and low toxicity, Fe_3O_4 NPs are widely employed as contrast agents in magnetic resonance imaging (MRI), enhancing diagnostic precision (Aram et al., 2022; Liu et al., 2020; Shen et al., 2018). Cancer cells are known to produce elevated levels of reactive oxygen species (ROS), in particular hydrogen peroxide (H_2O_2), compared to normal cells. This heightened oxidative state arises from increased metabolic activity and impaired mitochondrial function, contributing to tumour progression, angiogenesis, immune suppression and resistance to treatment (Palma et al., 2023). In this context, Fe_3O_4 NPs can catalyse Fenton-like reactions, converting H_2O_2 into highly reactive hydroxyl radicals (•OH) under acidic tumour microenvironment conditions. These radicals can cause oxidative damage to malignant cells, and amplify the therapeutic impact of Fe_3O_4 NPs (Dong et al., 2022).

Despite these advantages, a major limitation in therapeutic application of Fe_3O_4 NPs is achieving sufficient stability and dispersibility in biological environments. Without appropriate surface modifications, Fe_3O_4 NPs tend to aggregate, which significantly decreases their effectiveness in drug delivery. Prior studies, including our recently reported work (Moeni et al., 2024), have addressed the stability issues of Fe_3O_4 NPs to varying extents. Other reported studies (Aram et al., 2024; Jeshvaghani et al., 2022; Li et al., 2021) have focused on the functionalisation with polyethylene glycol (PEG) or amine groups which have been shown to enhance stability and prevent aggregation. However, challenges remain in designing robust NP formulations that simultaneously achieve optimal drug loading, stability, and therapeutic efficacy, particularly for chemotherapeutic agents, such as doxorubicin (DOX), docetaxel, paclitaxel, cisplatin, carboplatin, and oxaliplatin (OXA) (Yu et al., 2020). Although OXA is widely used in the treatment of digestive system cancers, and is capable of inducing immunogenic cell death, its efficacy as a monotherapy is often limited due to its poor selectivity, systemic toxicity, drug resistance, particularly in aggressive malignancies, such as breast, ovarian, and colon cancers (Wu et al., 2021; Zafar et al., 2021; Alcindor and Beauger, 2011; Yothers et al., 2011). These shortcomings underscore the urgent need for targeted delivery systems that can enhance index of OXA while minimising its systemic side effects (Zhang et al., 2022). Recent studies have explored the use of Fe_3O_4 NPs to improve the selectivity and delivery of OXA, offering promising methods to overcome some of the challengers (Liu et al., 2018; Kohan Hoosh Nejad et al., 2023; Wu et al., 2022; Chen et al., 2019). Tabasi et al (Tabasi et al., 2021). synthesised mesoporous pH responsive Fe_3O_4 NPs functionalised with amine groups and loaded with OXA to target CD44 receptors on HCT-116 colon cancer cells. Their findings demonstrated that the amine-functionalised Fe_3O_4 NPs catalysed the production of ROS and exhibited higher intracellular uptake compared to free OXA. This enhanced uptake may be attributed to electrostatic interactions between the positively charged amine groups and negatively charged CD44-proteins on the cancer cell (Tabasi et al., 2021).

Targeting specific subcellular components, in particular mitochondria, has emerged as a promising approach for boosting the efficacy of anti-cancer therapies. Mitochondria play a critical role in cellular metabolism and apoptosis, making them attractive target for therapeutic intervention (Prasun, 2019). Among different mitochondrial targeting ligands, triphenyl phosphonium groups, such as (3-carboxypropyl) triphenylphosphonium bromide (TPP), have been widely studied, since their introduction in 1969 for mitochondrial delivery application (Liberman et al., 1969). These cationic, lipophilic moieties exploit the high negative membrane potential across the inner mitochondrial membrane, a characteristic that is particularly pronounced in malignant cells (Smith et al., 2011; Xu et al., 2017a). This allows TPP-conjugated therapeutic agents selectively accumulate within the mitochondria of cancer cells, thereby increasing the specificity and potency of therapeutic agents (Sivagnanam et al., 2023; Jiang et al., 2021). Recent advances in nanotechnology have facilitated the incorporation of TPP with various nanocarriers to further improve the precision of mitochondrial targeting. For example, TPP has been conjugated to gold NPs for improved photodynamic therapying in breast cancer treatment, enabling precise mitochondrial targeting and enhanced therapeutic outcomes (Vinita et al., 2023). In another study (Hu et al., 2023), TPP was conjugated on the surface of mesoporous silica NPs (MSN) to enhance mitochondrial targeted delivery and enable synergistic therapeutic approach, combining copper depletion therapy and DOX for cancer treatment. The TPP moiety facilitated the efficient accumulation of the copper-chelating agent and DOX within the mitochondria, where their interaction led to increased ROS generation, and subsequent mitochondrial damage. This direct mitochondrial damage significantly compromised the energy metabolism of rapidly dividing malignant cells, ultimately resulting in their starvation and cell dearth (Hu et al., 2023). Sun et al. (Sun et al., 2018) demonstrated the potential of TPP-functionalised Fe_3O_4 NPs for co-delivering therapeutic agents. Kaneko et al. (Kaneko et al., 2023) engineered IONPs modified with TPP for application in magnetic hyperthermia. Their *in vitro* and *in vivo* studies exhibited that these TPP-conjugated IONPs effectively targeted mitochondria and induced effective subcellular thermal damage when exposed to alternating magnetic field, resulting in potent cytotoxic effects. The findings highlight the vital role of surface modification of IONPs, with TPP, in controlling intracellular localisation and enhancing the therapeutic efficacy of nanomedicine-based techniques (Kaneko et al., 2023). Despite these advances, there is limited work in the literature regarding the application of TPP-functionalised Fe_3O_4 NPs for the targeted delivery of chemotherapeutic agents. To date, to the best of our knowledge, there have been no reports on the use of TPP in conjunction with OXA-loaded Fe_3O_4 nanoparticles for cancer treatment.

This study addresses this gap by synthesising and characterising Fe_3O_4@MSN NPs functionalised with amine groups and conjugated with TPP, followed by OXA loading (Fe_3O_4@MSN-NH_2/TPP/OXA). A comprehensive suite of physical and analytical techniques was employed to characterise the synthesised NPs. *In vitro* cytotoxicity assay using the 3-(4, 5-dimethylthiazol-2-yl)-2,5-dipheynyltetrazolium bromide (MTT) were conducted on CT26 mouse colon cancer cells.

2. Materials and methods

2.1. Materials

Anhydrous iron (III) chloride ($FeCl_3$, AR grade), iron (II) sulfate heptahydrate ($FeSO_4.7H_2O$; AR grade), cetyltrimethylammonium bromide (CTAB, ≥96.0 %), tetraethyl orthosilicate (TEOS) (98 %), 3-aminopropyltriethoxysilane (3-APTES), N-hydroxysuccinimide (NHS, 98 %), TPP (98 %), phosphate buffer solution (PBS) and dimethyl sulfoxide (DMSO) were purchased from Sigma Aldrich. Ammonium hydroxide (NH_4OH 25–30 wt% in water; AR grade) was purchased from Merck. 1-ethyl-3-(3-dimethylaminopropyl) carbodiimide (EDCI), N-Methyl-2-pyrrolidone (NMP, 99 %) and acetate buffer (AcB) were purchased from Thermo Scientific. OXA was purchased from Molekula Group. Ethanol (70 %, AR grade) and High-Performance Liquid Chromatography grade water (HPLCW) were purchased from VWR International Ltd., UK. RPMI-1640 medium was purchased from Scientistic Laboratory Suppliers. Foetal calf serum (FCS) and Trypsin were purchased from Fisher Scientific Ltd., and CT26 cells were obtained from American Type Culture Collection.

2.2. Synthesis of Fe_3O_4 and preparation of Fe_3O_4@MSN-NH_2 nanoparticles

Fe_3O_4 NPs were synthesised *via* co-precipitation following the procedure reported in our previous work (Moeni et al., 2024), where we collected the synthetised Fe_3O_4 NPs in a wet paste form (WET) (50 % w/w). For the preparation of Fe_3O_4@MSN-NH_2, WET Fe_3O_4 NPs (1.0 g) were dispersed in HPLCW (120 ml) and ethanol (60 ml) and sonicated in an ice bath for 45 min. Subsequently, NH_4OH (1.2 ml) was added to the colloidal suspension and stirred for 1 h, at room temperature and under a nitrogen atmosphere. Next, CTAB (0.0729 g) was added dropwise to the solution, followed by the slow addition of TEOS (1.13 ml) via a syringe pump. The reaction mixture was stirred for 24 h (see Fig. 1. in Section 1 (S1), supplementary information 1(SI1). The resulting product (Fe_3O_4@CTAB-SiO_2) was washed with ethanol and HPLCW and collected using centrifuge and a magnet. Fe_3O_4@CTAB-SiO_2 (50 % w/w) was redispersed in anhydrous ethanol and sonicated. Then 3-APTES (1.2 ml) was added and stirred at room temperature for 24 h under N_2 flow for NH_2 functionalisation. The product Fe_3O_4@CTAB-SiO_2/NH_2 was rinsed with ethanol and collected using centrifugation and a magnet. To remove the CTAB, the product was refluxed in ethanol and NH_4NO_3 (6 mg/ml) for 8 h. The final product, Fe_3O_4@MSN-NH_2, was rinsed with water and ethanol and collected as wet paste (see Fig. 1 and Scheme 1, Stage 1).

2.3. Preparation of Fe_3O_4@MSN-NH_2/TPP

EDCI (2.250 mmol), NHS (2.170 mmol) and TPP (0.516 mmol) were dispersed in NMP (50 ml), and the reaction was allowed to run at room temperature for 24 h to activate the carboxylic group of TPP. Separately, Fe_3O_4@MSN-NH_2 wet paste (0.560 g) was dispersed in NMP then the pre-activated TPP solution was slowly added and stirred in the dark at room temperature for 48 h under a nitrogen atomsphere. The product was washed first with ethanol then with water and collected by centrifugation and a magnet, in a wet paste form (50 % w/w), (see Scheme 1, Stage 2).

2.4. Drug loading

2.4.1. Preparation of Fe_3O_4@MSN-NH_2/OXA

Fe_3O_4@MSN-NH_2 wet paste (0.560 g) was dispersed in HPLCW (10 ml) and sonicated in ice bath for 45 min, then transferred on a stirrer. Separately OXA (5 mg/ml) was dispersed in ethanol (5.63 ml) and sonicated for 5 min at 45 °C in the dark. The solution of OXA was added to the dispersed Fe_3O_4@MSN-NH_2 and the reaction was allowed

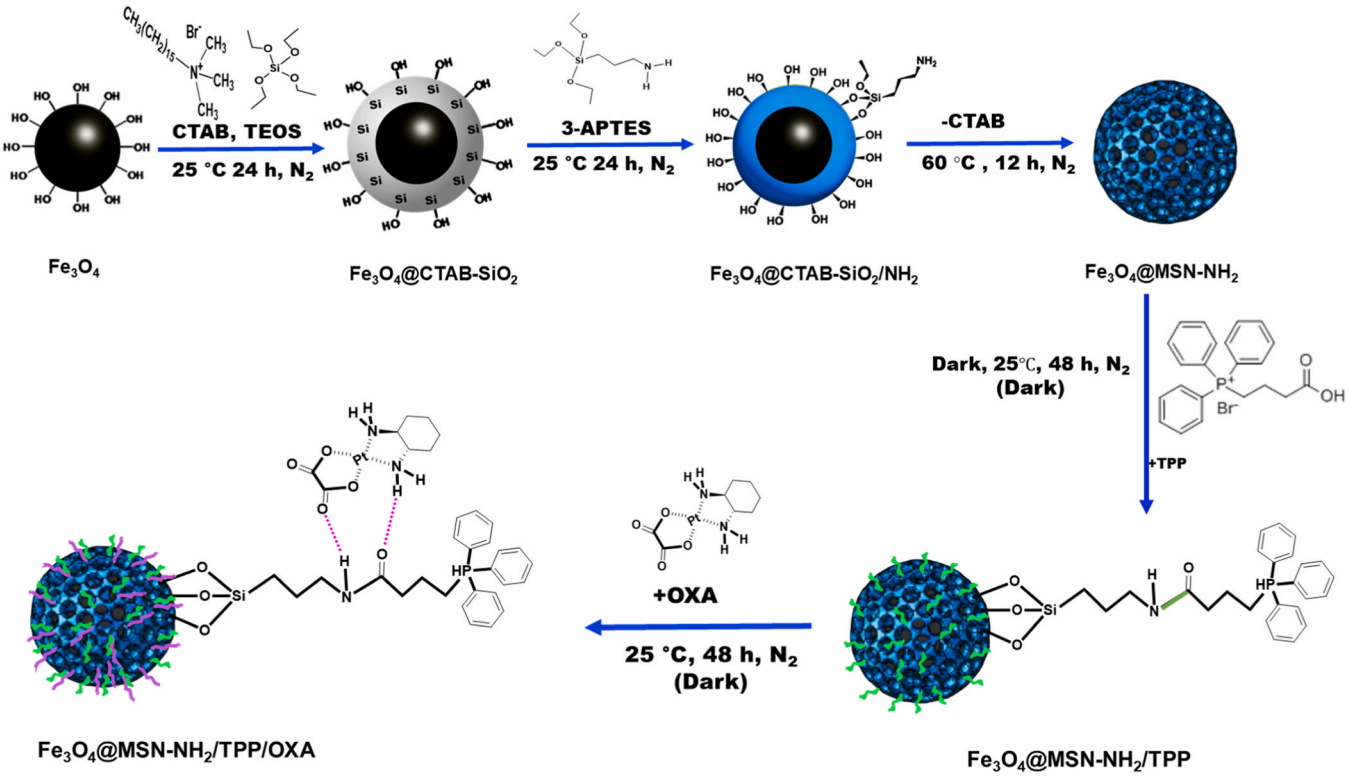

Fig. 1. Schematic illustrations of fabrication of Fe_3O_4@MSN-NH_2/TPP/OXA. Green and purple lines are the covalently bound TPP and the non-covalently bound OXA, respectively.

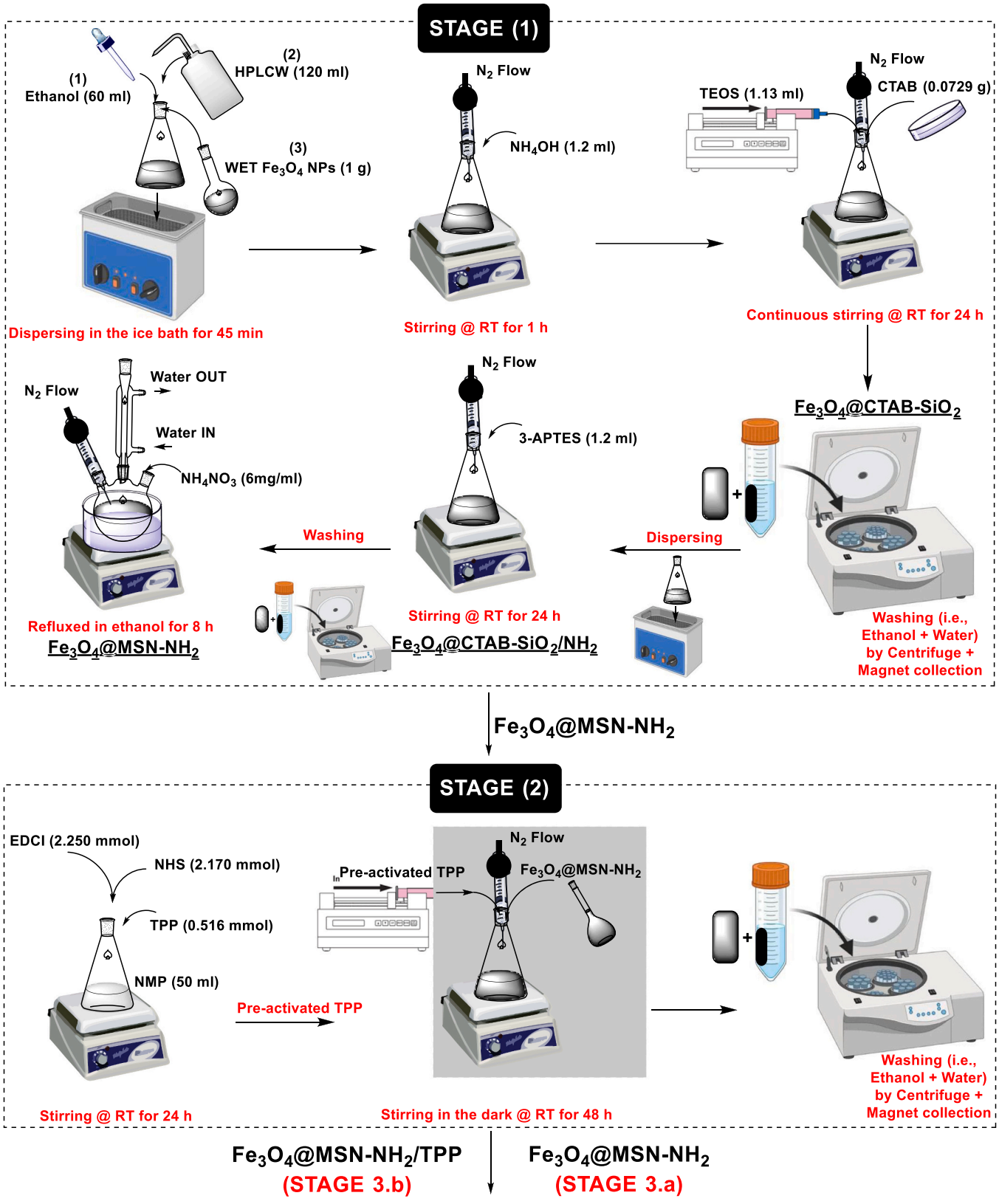

Scheme 1. Chemical process stages for preparation of Fe_3O_4@MSN-NH_2, Fe_3O_4@MSN-NH_2/OXA, Fe_3O_4@MSN-NH_2/TPP and Fe_3O_4@MSN-NH_2/TPP/OXA.

to run in the dark at room temperature for 48 h. The product was rinsed with HPLCW and collected by a permanent magnet in a wet paste form (50 % w/w), (see Scheme 1, Stage 3.a).

2.4.2. Preparation of Fe_3O_4@MSN-NH_2/TPP/OXA

Fe_3O_4@MSN-NH_2/TPP wet paste (0.560 g) was dispersed in water (60 ml) and sonicated for 45 min in an ice bath, then transferred on the

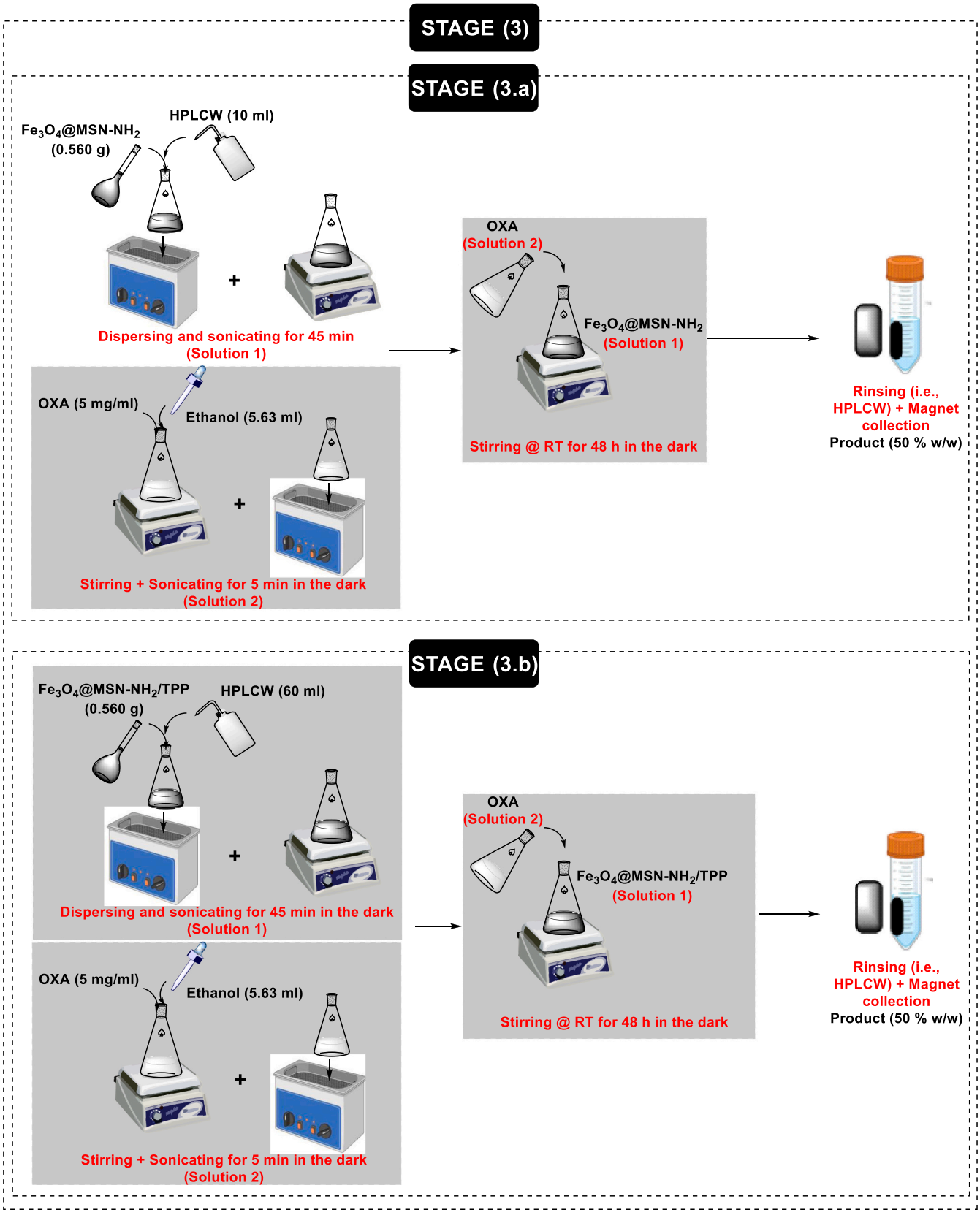

Scheme 1. (*continued*).

stirrer in the dark. Separately, OXA (5 mg/ml) was dispersed in ethanol (5.63 ml) and sonicated for 5 min at 45 °C in the dark. The solution of OXA was added to dispersed Fe_3O_4@MSN-NH_2/TPP and the reaction was allowed to run in the dark at room temperature for 48 h. The product was rinsed with HPLCW and collected by a permanent magnet in a wet paste form (50 % w/w), (see Scheme 1, Stage 3.b).

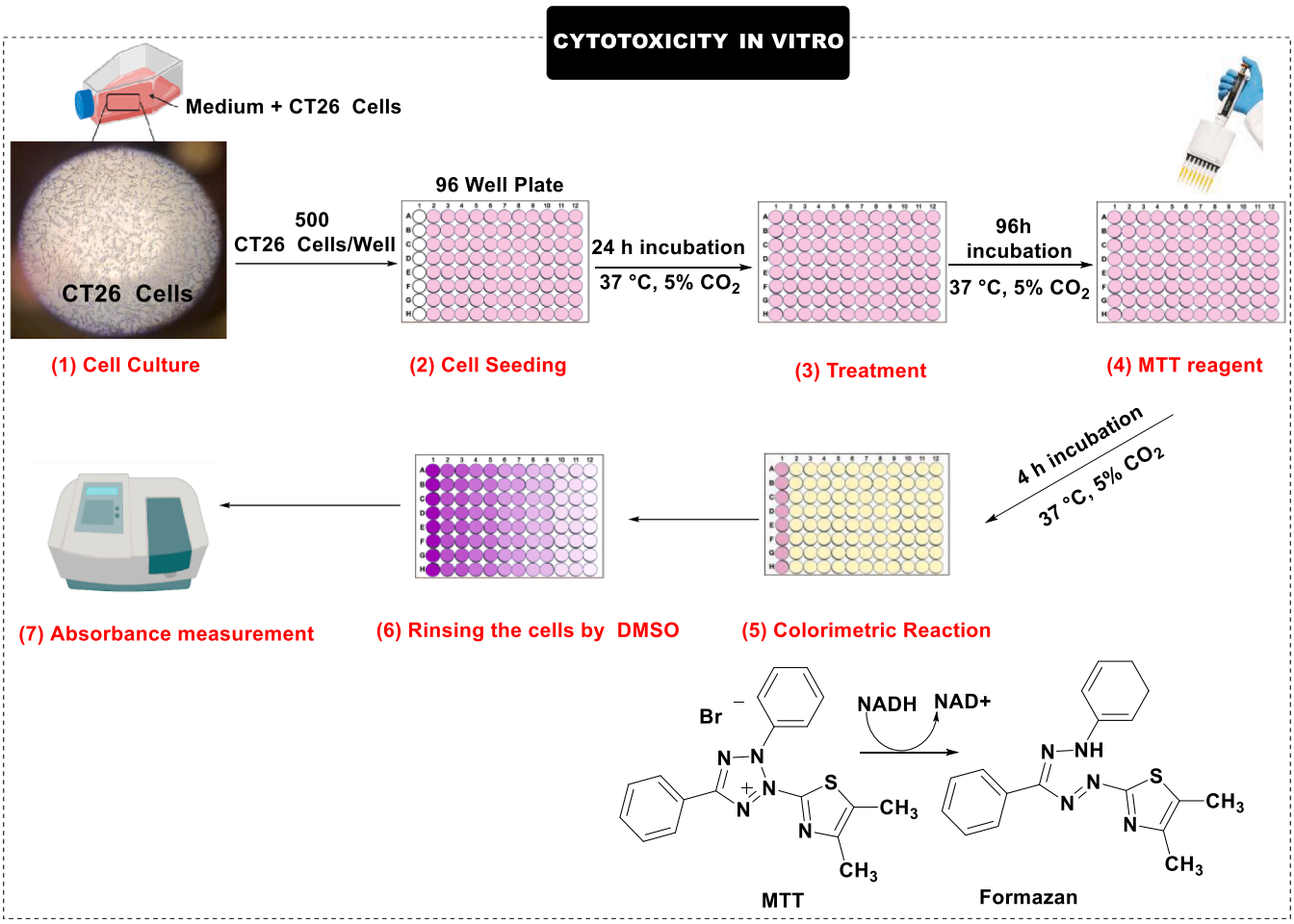

Scheme 2. Process of cytotoxicity test *in vitro* of Fe_3O_4@MSN-NH_2, Fe_3O_4@MSN-NH_2/OXA, Fe_3O_4@MSN-NH_2/TPP and Fe_3O_4@MSN-NH_2/TPP/OXA.

2.5. Characterisation techniques

A Bruker Vertex 80 V Fourier Transform infrared (FT-IR) spectrometer applying the attenuated total reflection (ATR) was used to identify the functional groups in the range of 4000–650 cm^{-1}, at resolution of 4 cm^{-1} by conducting 32 scans. The detector was RT-DLaTGS with the sampling accessory of Bruker A225/Q Platinum single-bounce ATR with diamond crystal. The structural and crystal phase analyses of the NPs were investigated by Bruker D2 Phaser Powder X-ray diffraction (PXRD) with Cu-Kα radiation (λ=1.541 Å) and a LinxEye detector. The operating voltage was at 40 kV and with an applied current of 40 mA. All the samples were scanned in the angular range of $5^\circ \leq 2\theta \leq 80^\circ$ and exposure time of 10 s and total measurement time of 11 h. The surface morphologies and elemental composition of the NPs were assessed, using FEI Tecnai TF20 FEGTEM Field emission gun TEM/STEM fitted with high annular dark-field imaging (HAADF) detector, Oxford Instruments INCA 350 EDX system/80 mm X-Max SDD detector and Gatan Orius SC600A CCD camera. A droplet of dispersed NPs in HPLCW was injected on a carbon-coated copper grid for the morphology and elemental composition analyses. The dynamic light scattering (DLS) for hydrodynamic size (D_H) and zeta potential (ZP) for particle charge of the NPs in the solutions were investigated using Zetasizer (Nano ZSP ZE5600, Malvern Instruments Ltd, UK). For the preparation, the NPs (0.1 mg/ml) were dispersed in HPLCW and homogenised by Fisher Scientific™ FB705 sonic Dismembrator ultra-sonic probe transferred in a disposable cuvette for examination. Dispersion stability of IONPs were measured by LUMiSizer. The specification of dispersion analyser was LUMiSizer 6112–29, 12 channels, rota radius (10 cm) equipped with SEPView® software, ADAPTIVE INSTRUMENTS, Germany. The stability of the dispersed IONPs were measured at wavelength of 865 nm with minimum and maximum light factors of 0.25 and 6, respectively. For preparation, the samples were dispersed in PBS (0.1 mg/ml) and sonicated in ice bath for 45 min, then transferred (1 ml) into an optical LUMiSizer cuvette and centrifuged at 3000 rpm for 3000 s at different temperatures (4 °C, 25 °C, 37 °C, 43 °C, the temperatures at which the therapeutic agent was stored, under ambient temperature, human body temperature and magnetic hyperthermia conditions, respectively). Superconducting quantum interference device vibrating sample magnetometer (VSM) at 300 K, and magnetic field of 7 Tesla (T) was used to study the magnetic properties of the dried NPs. The amount of OXA loading was measured by inductively coupled plasma optical emission spectrometer (ICP-OES, Thermo Scientific iCAP7400 radial, USA) with autosampler Cetac ASX-520, software Thermo Qtegra, Quartz Seaspray nebuliser and Quartz cyclonic spray chamber.

The accumulation percentage of OXA was quantified using an Agilent 1290 Infinity II HPLC system (Agilent, Santa Clara, CA, United States), with a diode array detector (DAD). Chromatographic separations were performed using an Agilent InfinityLab Poroshell 120 EC-C18 (2.1 ×50 mm, 1.9 μm) at a column temperature of 40 °C. The mobile phase used was 0.1 % Trifluoroacetic acid in water (95 %) and 0.1 % Trifluoroacetic acid in acetonitrile (5 %) and the gradient running to 5 % water over 5 min at a flow rate of 0.5 ml/min. The DAD recorded the chromatogram at a wavelength of 254 nm. The elemental composition and electronic state of the samples were studied by ultra-high vacuum (UHV) X-ray photoelectron spectroscopy (XPS) using a SPECS FlexMod UHV-XPS. It has a SPECS Phoibos 150 hemispherical analyser with 1D-DLD detectors. The source is a monochromated Al k-alpha with a photon energy at 1486.7 eV and a power of 400 W and 15 kV. The

vacuum is around 1×10^{-9} mbar. An electron flood gun is used to charge neutralise the sample during measurement. The sample preparation was performed by pressing the powder onto the tape attached to an omicron sample plate. The surface area and the porosity of the samples were measured by a Brunauer-Emmett-Teller (BET) adsorption-desorption facility (Nova 800 series, Austria) with Anton Paar Kaomi for Nova software.

2.6. Drug release test

The release profile of OXA from Fe_3O_4@MSN-NH_2/OXA and Fe_3O_4@MSN-NH_2/TPP/OXA at different time intervals were investigated. Each sample (2 mg/ml WET paste, (50 % w/w) was re-dispersed in two different pH environments (PBS, pH 7.4 and AcB, pH 5.0) and sonicated for 45 min in an ice bath (to avoid overheating during sonication). The samples were added into a dialysis bag (MWCO=3500 Dalton), stirred at 37 °C for 48 h. Solution was collected at different time intervals (3, 6, 9, 12, 24, 36 and 48 h) and the amount of OXA release was measured by HPLC-UV.

2.7. MTT cytotoxicity assay

CT26 mouse colon cancer cells were cultured in medium (RPMI, 10 % (v/v) heat inactivated FCS) at 37 °C in a humidified atmosphere containing 5 % CO_2. Cells were harvested, counted and seeded at a density of 500 cells/well (low cell density) in a 96 well-plate followed by 24 h incubation at 37 °C in a humidified atmosphere containing 5 % CO_2. Fe_3O_4@MSN-NH_2, Fe_3O_4@MSN-NH_2/OXA, Fe_3O_4@MSN-NH_2/TPP and Fe_3O_4@MSN-NH_2/TPP/OXA samples were dispersed in culture medium (0.5 mg/ml) and sonicated for 45 min in ice bath. Serial dilutions of free OXA or NPs were prepared in culture medium. The cells were treated with carrier control or a range of drug/particle concentrations for 96 h. The MTT stock solution (5 mg/ml in PBS) was then added (20 µl/well) to the cells and incubated for 4 h. The media was removed, and 150 µl of DMSO were added. Once the crystals were fully dissolved the absorbance was measured at 620 nm using Cytaiton 5 Imaging Plate Reader (BioTek, United States). Statistical analysis was performed in Prism 9, using 2-way ANOVA test with Geisser-Greenhouse correction.

3. Results and discussion

In this study, Fe_3O_4@MSN-NH_2/TPP/OXA NPs were synthetised according to the method displayed in Fig. 1. Initially, the core Fe_3O_4 NPs were fabricated using co-precipitation reaction which is reported in our previous work (Moeni et al., 2024). The Fe_3O_4 NPs then were coated via traditional sol-gel reaction and functionalised with -NH_2 groups, followed by conjugation of TPP and loaded with OXA.

3.1. Physical and analytical properties

FT-IR spectra (Fig. 2 **(a))** show the stepwise surface functionalisation of Fe_3O_4@MSN-NH_2, verifying the successful conjugation with TPP and OXA. The appearance of broad absorption band between ~3550–3200 cm^{-1}, is a convolution arising from overlapping O-H and N-H stretching vibrations. The O-H stretching attributed to the residual surface silanol groups (Si-OH) and adsorbed water, while N-H signals originate from the primary amines attached through salinisation process

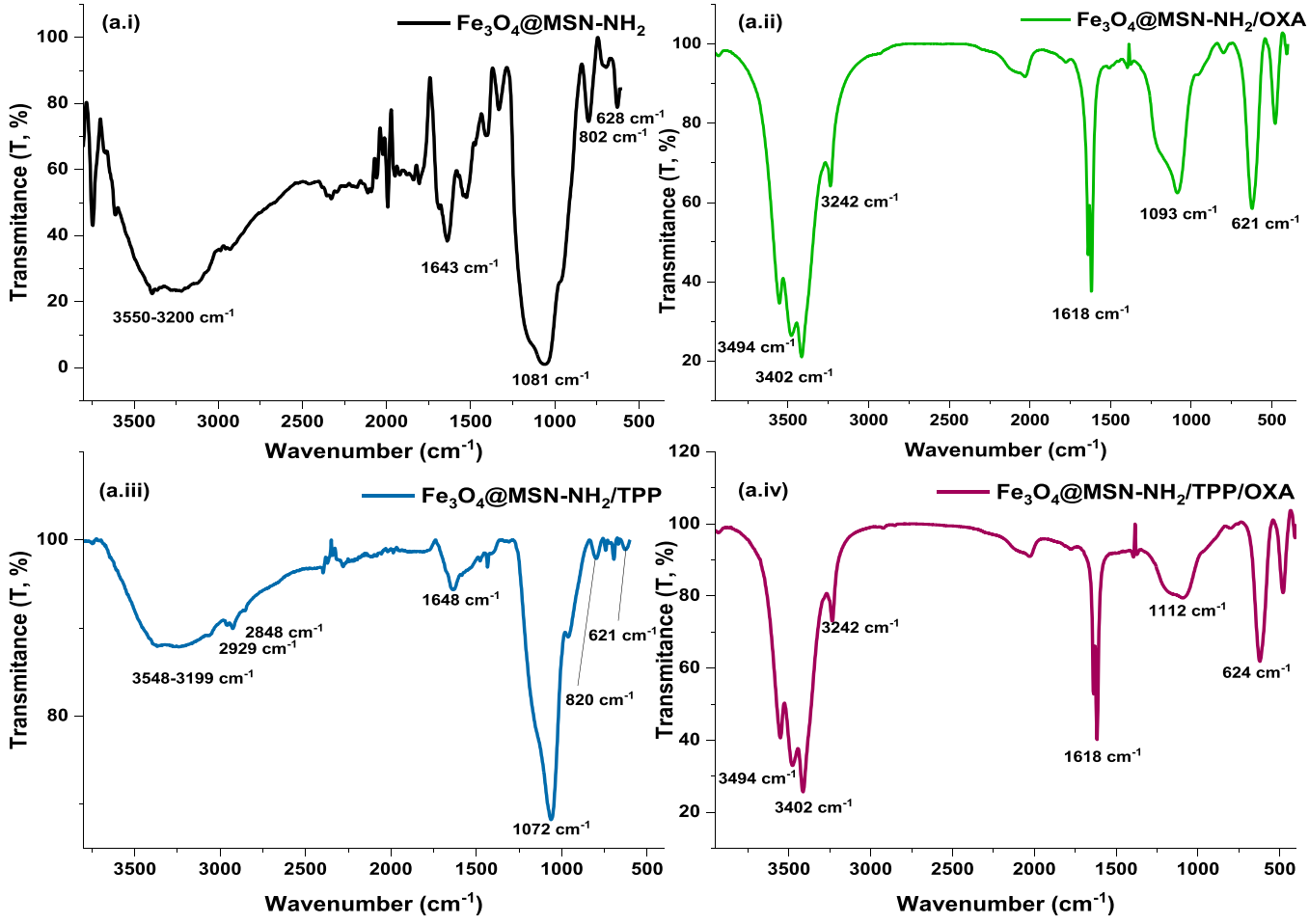

Fig. 2. FT-IR spectra: (a.i) Fe_3O_4@MSN-NH_2, (a.ii) Fe_3O_4@MSN-NH_2/OXA, (a.iii) Fe_3O_4@MSN-NH_2/TPP, and (a.iv) Fe_3O_4@MSN-NH_2/TPP/OXA.

with 3-APTES. This band confirms the presence of hydroxyl and amine groups, enabling the subsequent surface functionalisation (Fig. 2 **(a.i)**). The results are atypical for mesopores silica coating, parallel with the findings in the literatures (Grisolia et al., 2024; Mudhakir et al., 2024; Estevão et al., 2021). The absorption peak at 1643 cm^{-1} corresponded to N-H bending, attributed with primary amine groups of 3-APTES (Fig. 2 **(a.i)**). This spectral behaviour aligns well with recent literature, for example Petreanu et al. (Petreanu et al., 2022) reported a bending between 1600 and 1650 cm^{-1} regions, confirming the effective amine coating (Petreanu et al., 2022). The incorporation of silica shell and Fe_3O_4 core is evidenced by the sharp adsorption peak between 1089 cm^{-1}-1100 cm^{-1} which is attributed to Si-O-Si asymmetric stretching, while the symmetric stretching appears around 802 cm^{-1} regions and Fe-O vibrations appears at ~620 cm^{-1} (Fig. 2 **(a.i)**). Following functionalisation with TPP (Fig. 2 **(a.iii)**), the absorption bands appear at 2929 cm^{-1} and 2848 cm^{-1}, attributed to the asymmetric and symmetric C-H stretching vibrations in methylene groups (-CH_2) of TPP, suggesting successful TPP functionalisation. The original N-H band at 1643 cm^{-1} shift slightly to high frequency (1648 cm^{-1}), however this was not sufficient to confirm the formation of covalent bonding between the surface -NH_2 groups and TPP's -COOH groups through EDCI-NHS (coupling agents) mediated amide bond. Further analysis by XPS is required in this regard. Upon OXA loading in Fig. 2 (a. ii) and (a.iv) respectively, a new absorption peak emerges at 1618 cm^{-1}, corresponding to the C═O stretching vibration of carbonyl groups in OXA. Additionally, this band's proximity to the original N-H bending (1643 cm^{-1}) might indicate the participation of N-H bond in the formation of possible H-bonding between surface -bound -NH_2 groups and oxygen of OXA. It may also be a weak coordination interaction between the lone pair electrons on nitrogen of surface bond -NH_2 groups with platinum centre of OXA, forming a coordination bond. This interaction may have affected the electron density around the original N-H, leading to shift in low frequency, either way it confirms the successful loading of OXA. Medium intensity peaks between 3242 and 3402 cm^{-1} are assigned to aliphatic primary amine, originated from the OXA structure. The presence of these peaks, absent in both Fe_3O_4@MSN-NH_2 and Fe_3O_4@MSN-NH_2/TPP suggests successful incorporation of OXA into the IONPs. The details of frequency assigned, and the wavenumbers are collected in Table 1.

XPS analysis was performed to identify the chemical composition of Fe_3O_4@MSN-NH_2, Fe_3O_4@MSN-NH_2/OXA, Fe_3O_4@MSN-NH_2/TPP and Fe_3O_4@MSN-NH_2/TPP/OXA. The XPS survey showed the presence of C, O, N, Si and Fe in all four samples (the results are displayed in SI1 (Fig. 2 (S2a)). Additionally, the XPS results of as received OXA and TPP, are provided in the SI1 (Fig. 2(S2b). Fig. 3 (a and b) displays the high-resolution spectra (O 1 s, P 2p and Pt 4 f), peak deconvolution, and the fitting envelopes of Fe_3O_4@MSN-NH_2/TPP and Fe_3O_4@MSN-NH_2/TPP/OXA. The peak at 531.20 eV (spectrum a.i) is most likely associated with oxygen species in TPP loaded sample which suggests the formation of amide bonds, upon covalent binding of TPP (refer to Fig. 1 for clarification) (Beamson and Briggs, 1992). While in Fe_3O_4@MSN-NH_2/TPP/OXA sample, the loading of OXA created additional oxygen environments which correspond to O 1 s peaks. The appearance of a new peak (peak b.i) at 535.18 eV is due to the oxygen species of C═O in oxalate ligand indicating the successful loading of OXA (Beamson and Briggs, 1992; Henderson et al., 2025). Moreover, in Fig. 3(b.ii) the Pt 4 f peaks are deconvoluted into two peaks at 73.39 eV and 76.73 eV which corresponded to Pt 4 $f_{5/2}$ and Pt 4 $f_{7/2}$ peaks respectively. This is similar to platinum phthalocyanine (Yakushi et al., 1991) which makes sense for the OXA due to the bonds between the nitrogen and platinum. Fig. 3(a.ii) shows the P 2p spectra for the Fe_3O_4@MSN-NH_2/TPP sample with the main P 2p 3/2 peak at 133.2 eV and a smaller set of peaks (15 %) with the P 2p 3/2 peak at 134.95 eV. These binding energies are substantially higher than typical binding energy for unoxidised TPP (~131.0 eV). This discrepancy indicates that the P environment within the sample might have undergone oxidation, most plausibly forming TPPO or other oxidised species. The reaction was carried out under inert environment (N_2 flow), ambient temperature and in an aprotic solvent (NMP). Recent studies on TPP has demonstrated that TPP can be oxidised to TPPO even under mild conditions (Stewart et al., 2023; Wind et al., 2024). In this study, several factors may have attributed for this transformation. Fe_3O_4 NPs are known for their redox-active surface (Fe^{2+} and Fe^{3+}), which can provide surface-mediated electron transfer reactions, promoting mild oxidation of adsorbed or surface-associated species (Dong et al., 2022; Sharma et al., 2024). Other factors such as the use of coupling agents, EDCI and NHS produce reactive intermediate (e.g. O-acylisourea), which may have interacted with nucleophilic phosphorous centre of TPP. Although, NHS stabilises the intermediate, side reactions may have been generated, due to the presence of catalytic surface such as Fe_3O_4 and the polar aprotic NMP may have enhanced their surface interactions.

The high-resolution transmission electron microscopy (HR-TEM), HAADF-SEM, and Energy dispersive x-ray spectroscopy (EDX) images are taken to study the morphology and chemical compositions of synthetised NPs at different stages. For comparison TEM characterisation data for Fe_3O_4@MSN-NH_2, Fe_3O_4@MSN-NH_2/OXA, and Fe_3O_4@MSN-NH_2/TPP NPs are provided in the SI1, Fig. 3(S3). The HR-TEM images of Fe_3O_4@MSN-NH_2/TPP/OXA NPs are displayed in Fig. 4(a.i-a.iv). The TEM images showed the mean diameter of primary particles (D_{TEM} (nm)) is 14 ± 2 nm (Fig. 4(a.i) and particles exhibited spherical to quasi-polyhedral shapes. The size of the largest aggregate in the Fe_3O_4@MSN-NH_2/TPP/OXA samples, is less than 60 nm (Fig. 4(a.ii)), which is suitable for the targeted drug delivery (TDD), also is within the range of superparamagnetism (a phenomenon which will be explained later). Selected area diffraction pattern (SAED) spectra displayed a set of diffraction rings (Fig. 4(b)) consistent with the crystal planes at (111), (220), (311), (400), (422), (511), (440) and (533) of Fe_3O_4 NPs results (in line with reports in the literature (Moeni et al., 2024; Radoń et al., 2017). The observed lattice fringes corresponded to the (220) crystallographic plane of Fe_3O_4 with an interplanar spacing of ~0.293 nm. This

Table 1
FT-IR spectral analysis of NPS samples.

Frequency assigned	Fe_3O_4@MSN-NH_2	Fe_3O_4@MSN-NH_2/OXA	Fe_3O_4@MSN-NH_2/TPP	Fe_3O_4@MSN-NH_2/TPP/OXA
	Wavenumber (cm^{-1})			
O-H	3550–3200 cm^{-1} strong-broad stretch Alcohol Intermolecular bonded	-	3548–3199 cm^{-1} strong-broad stretch Alcohol Intermolecular bonded	-
N-H	1643 cm^{-1} Bending amine	3402 cm^{-1}, 3242 cm^{-1} Medium stretch aliphatic primary amine	1637 cm^{-1} Bending amine	3402 cm^{-1}, 3230 cm^{-1} Medium stretch aliphatic primary amine
C═O	-	1618 Strong stretch	-	1618 Strong stretch
Si-O-Si	1081	1093	1072	1112
Fe-O	628	626	621	624

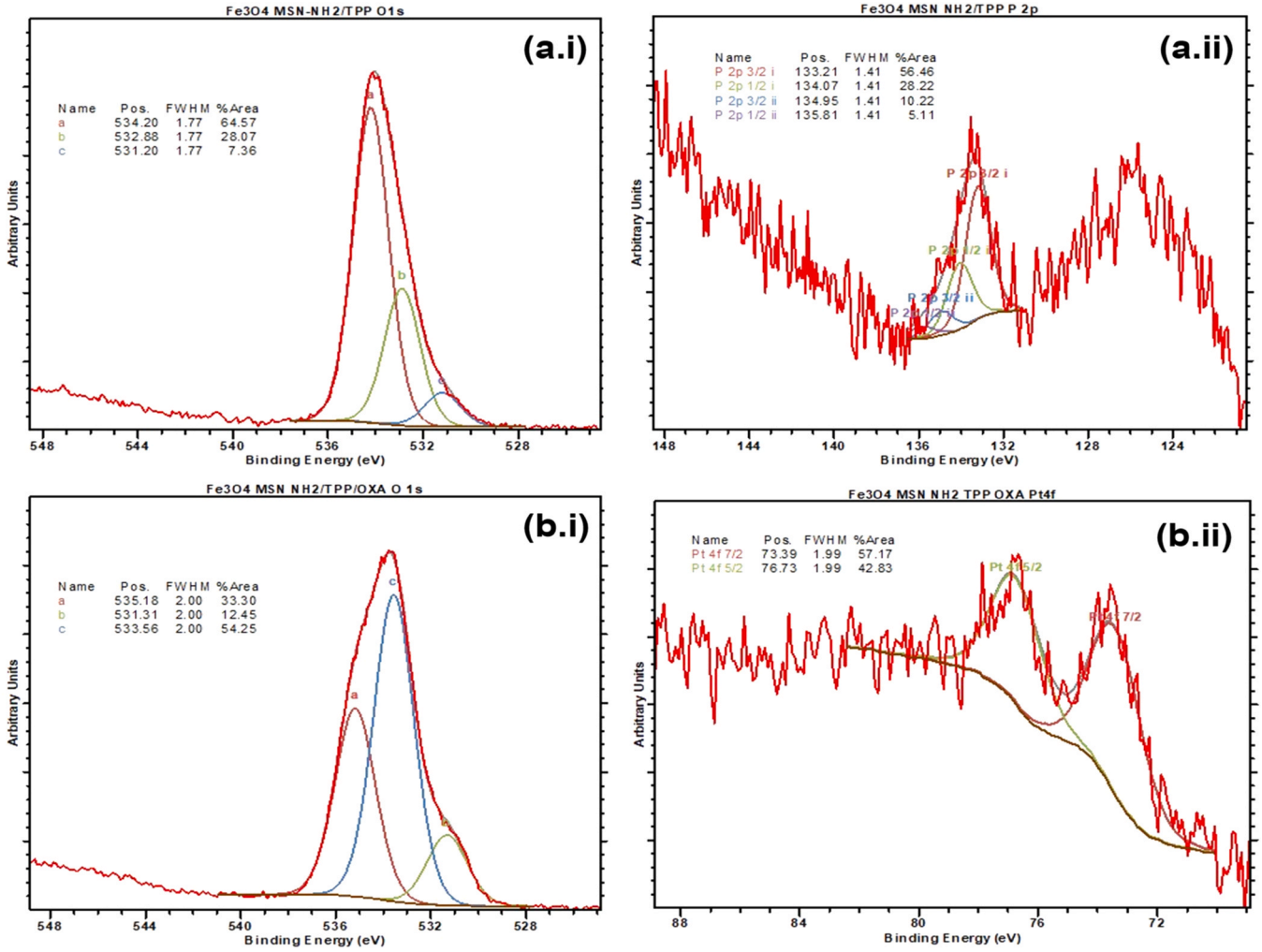

Fig. 3. XPS spectra: **(a.i)** O environment and, **(a.ii)** P environment of Fe_3O_4@MSN-NH_2/TPP, **(b.i)** O environment, and **(b.ii)** Pt environment of Fe_3O_4@MSN-NH_2/TPP/OXA.

conformed the core maintained its crystallographic structure even after surface functionalisation and OXA loading (Fig. 4(a.iii).

The EDX mapping images in Fig. 4, (d.i-d.v) validate the core-shell structure, of Fe_3O_4@MSN-NH_2/TPP/OXA NPs. Fig. 4(d.i) exhibits the elemental distribution of Fe, Si, and Pt, clearly showing Fe concentrated in the core and Si formed a shell around it, suggesting a well-defined core-shell structure which complement the HR-TEM image shown in Fig. 4(a.iv). Moreover, Fig. 4(d.ii) displays HAADF image which serves as a base image for (d.i) to assist visualisation of morphology and structural feature of core-shell framework. Fig. 4(d.iii) highlights the Fe-rich core, while Fig. 4(d.iv) Si, emphasises the Si shell and Fig. 4(d.v) demonstrates the presence of Pt. According to the EDX spectra (Fig. 4 (e)), the phosphorous (P) signals appear to be masked by the dominant Si signal from mesoporous SiO_2 shell. This is likely due to the close energy levels of their Kα X-ray emission peaks (P Kα1 ~2.01 keV and Si Kα1 ~1.74), as well as their relatively low atomic numbers, which make it challenging to differentiate them using EDX analysis. In regard to Pt, the EDX mapping clearly suggests that OXA was successfully incorporated into the Fe_3O_4@MSN-NH_2/TPP structure. The Pt appears to be uniformly distributed and predominantly resided within the MSN matrix. The significant overlap of the Pt signals with Si, rather than Fe implied that the OXA was adsorbed in/onto the mesoporous silica shell an optimal site for drug delivery.

PXRD was used to study the crystallite size, and d-spacing of the Fe_3O_4@MSN-NH_2, Fe_3O_4@MSN-NH_2/OXA, Fe_3O_4@MSN-NH_2/TPP, and Fe_3O_4@MSN-NH_2/TPP/OXA samples (Fig. 5). In Fe_3O_4@MSN-NH_2 a broad hump between $2\theta = 20°$-$22°$ was observed, attributed to the amorphous SiO_2 shell, consistent with previous reports (Khalid et al., 2023; Divya et al., 2022). All samples demonstrated diffraction peaks that matched well with the characteristic (hkl) planes and d-spacings of cubic Fe_3O_4 crystal phase, as referenced in the JCPDS standard card No. 00–026–1136 (Moeni et al., 2024). A Comparison of PXRD parameters between JCPDS data and the synthesised samples is provided in the SI1 (S4, Table 1). Lattice parameters were calculated using Bragg's diffraction angle (θ), and the full width at half maximum (β, FWHM) of the most intense (311) diffraction peak, fitted using applying Lorentz fitting.

According to Braggs' law (Cullity and Stock, 2001);

$$n\lambda = 2d\sin\theta \quad (1)$$

where n is the diffraction order, λ is the PXRD wavelength and d is the spacing between planes of Miller indices h, k, and l. The average crystallite size $D_{(311)}$ of NPs was calculated using the Debye-Scherer's equation (Moeni et al., 2024);

$$D_{(311)} = K\lambda/\beta\cos\theta \quad (2)$$

The average crystallite sizes of Fe_3O_4 in Fe_3O_4@MSN-NH_2, Fe_3O_4@MSN-NH_2/OXA, Fe_3O_4@MSN-NH_2/TPP, and Fe_3O_4@MSN-NH_2/TPP/OXA NPs, as calculated from the (311) PXRD peak applying the Scherrer equation, were approximately 8.6 nm, 7.6 nm, 8.0 nm, and

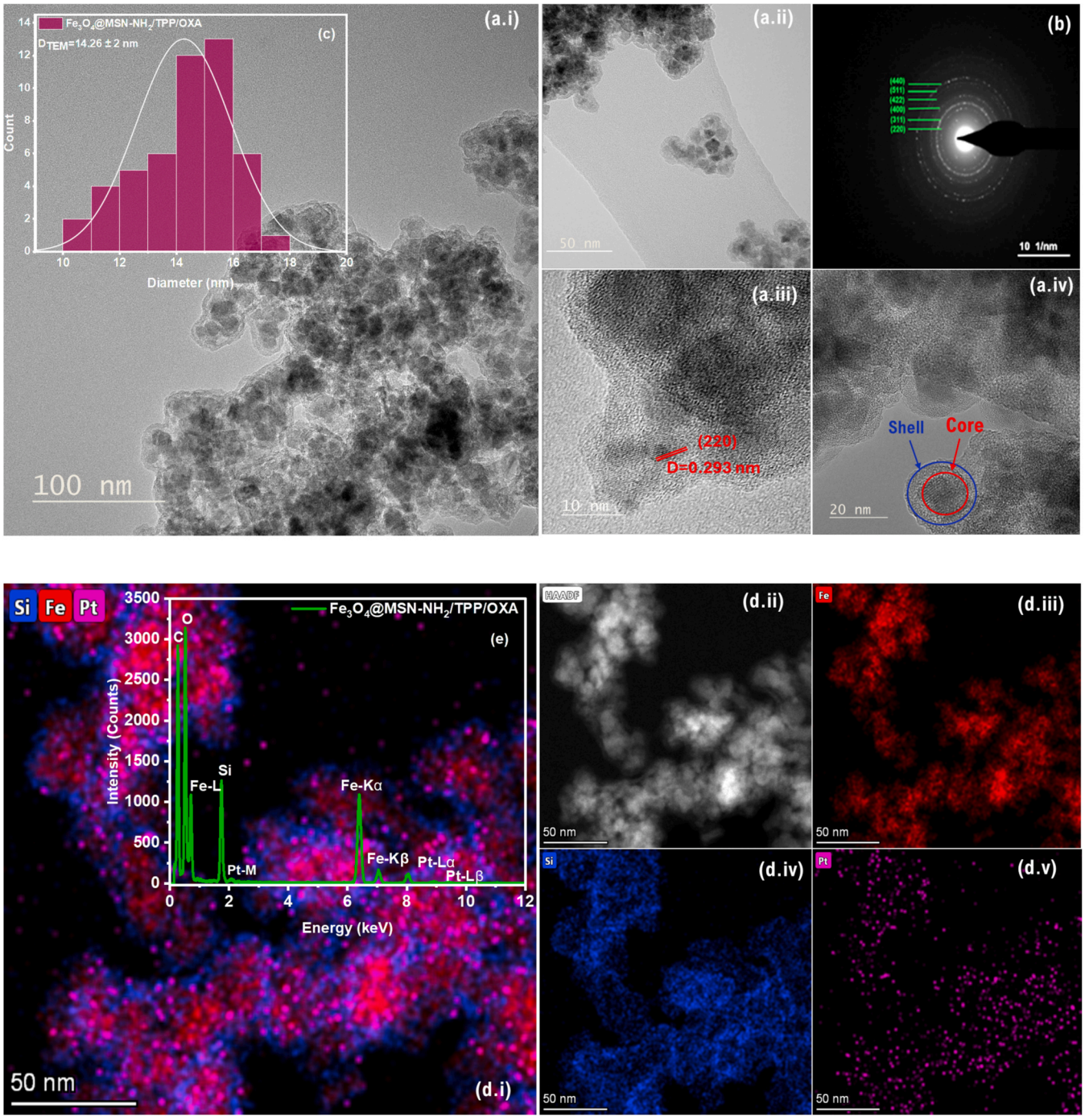

Fig. 4. High-Resolution TEM images (HR-TEM) of Fe_3O_4@MSN-NH_2/TPP/OXA, (a.i) HR-TEM, (a.ii) and (a.iii) Zoomed view, (a.iv) SAED Pattern, (c) particle size distribution, (d.i) EDX mapping, core-shell structure, (d.ii) HAADF, (d.iii) iron (Fe), (d.iv) silica (Si), (d.v) platinium (Pt), (e) EDX spectra (Cu is from the cupper grid).

9.3 nm, respectively. These results suggest minimal variation in Fe_3O_4 core size across various surface modification stages which is consistent with HR-TEM observations.

Also, internal micro-strain (ε), which represents the degree of distortion/strain due to stress and dislocation density (δ), reflecting the number of defects in a per unity area of the crystal structure can influence the physical and chemical properties of the samples (Sánchez-Bajo et al., 2008). Both (ε) and (δ) can be estimated via the followings;

$$\varepsilon_{(311)} = \beta_{(311)}/4\tan\theta \quad (3)$$

$$\delta_{(311)} = 1/D^2_{(311)} \quad (4)$$

As shown in Table 2, the overall impact of dislocation density (δ) and internal micro-strain (ε) on the structural integrity of all samples were minimal; the samples remained stable and crystalline. This further validates that the Fe_3O_4 core was not significantly altered by the modification treatments, the findings aligns with the Scherrer's equation values and HR-TEM.

Specific surface areas of Fe_3O_4@MSN-NH_2, Fe_3O_4@MSN-NH_2/OXA, Fe_3O_4@MSN-NH_2/TPP and Fe_3O_4@MSN-NH_2/TPP/OXA was determined by BET nitrogen adsorption-desorption method. According to Abmroz et al. (Ambrož et al., 2018) and Sheilds et al. (Shields et al., 2006) the reliable BET measurements needs careful degassing to remove all phsisorbed contaminants, in particular water and residual gases from

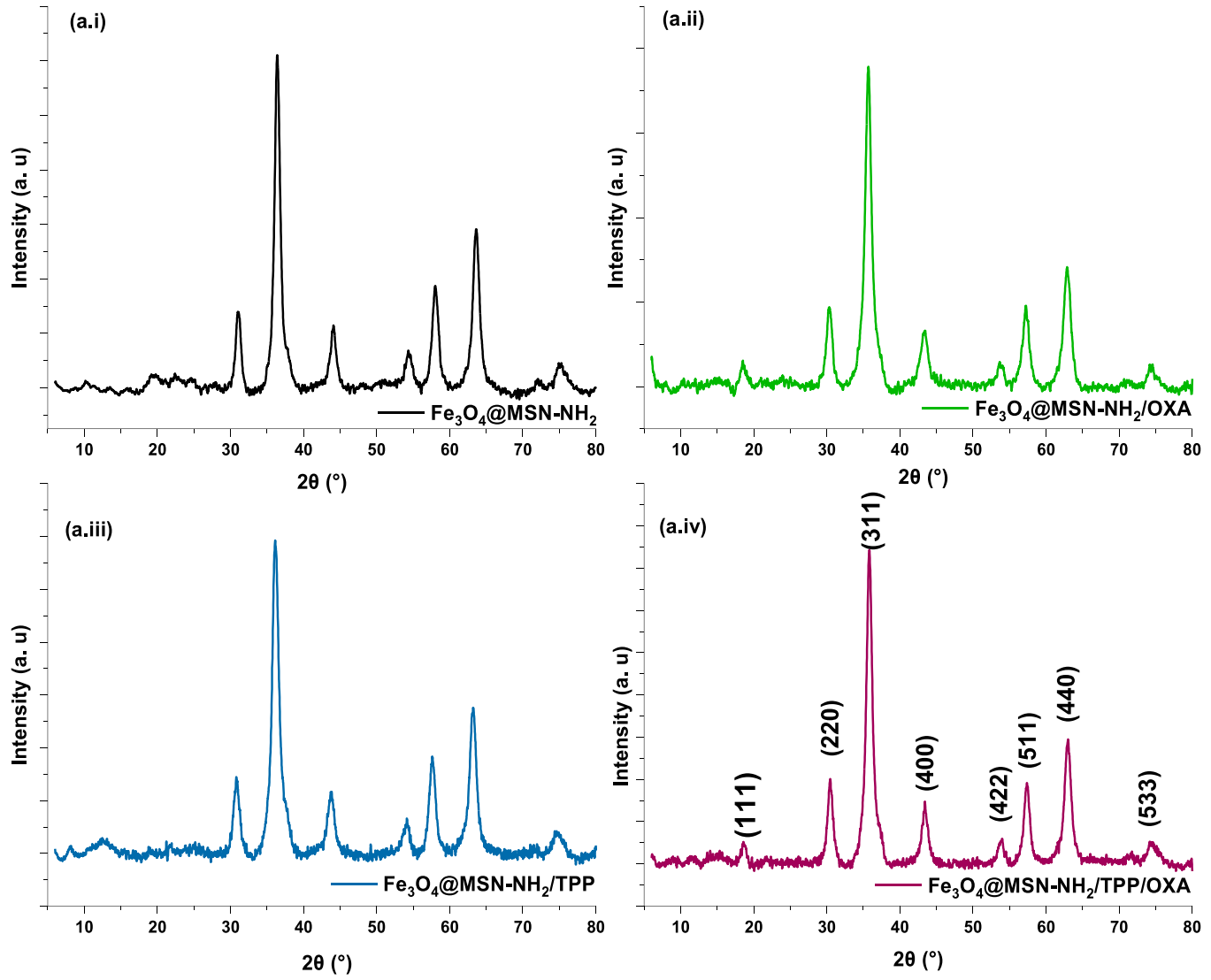

Fig. 5. PXRD spectra of (a.i) Fe_3O_4@MSN-NH_2, (a.ii) Fe_3O_4@MSN-NH_2/OXA, (a.iii) Fe_3O_4@MSN-NH_2/TPP, and (a.iv) Fe_3O_4@MSN-NH_2/TPP/OXA.

Table 2
PXRD parameters of samples.

PXRD Parameters	Fe_3O_4@MSN-NH_2	Fe_3O_4@MSN-NH_2/OXA	Fe_3O_4@MSN-NH_2/TPP	Fe_3O_4@MSN-NH_2/TPP/OXA
FWHM $\beta_{(311)}$ (°)	0.89	1.10	1.05	0.94
d-spacing (Å)	2.47	2.48	2.52	2.50
$D_{(311)}$ (nm)	8.58	7.55	8.00	9.30
$\delta_{(311)}$ (nm^{-2})	1.042×10^{-2}	1.447×10^{-2}	1.016×10^{-2}	1.161×10^{-2}
$\varepsilon_{(311)}$	1.281×10^{-3}	1.474×10^{-3}	1.572×10^{-3}	1.327×10^{-3}

Interplanar spacing (d-spacing, (Å)), the average particle size ($D_{(311)}$ (nm)), internal micro-strain (ε), dislocation density (δ)

the surface and pores. Inadequate degassing leads to inaccurate surface area and pore volume analysis, as the adsorbate molecules (e.g., nitrogen) would compete with residual species for adsorption sites (Ambrož et al., 2018). To ensure accuracy, all samples were initially heated to 60 °C at 5.0 °C/min and held for 60 min, followed by elevating the temperature to 100 °C at the same rate and held for 900 min prior to BET measurements at 77 K. As shown in Fig. 6(a and b), all samples displayed type IV isotherm, with H1-type hysteresis loops, known nature for mesoporous species with cylindrical pores. A minor contribution of micropores was also observed. The BET parameters are collected in Table 3. The base sample, Fe_3O_4@MSN-NH_2, displayed the highest surface area (419.95 m^2/g), and the largest micropore volume (0.086 cm^3/g), confirming a well-designed mesoporous structure. Following loading OXA, the BET surface area and micropore volume decreased to 189.06 m^2/g and 0.019 cm^3/g, respectively, while BET particle diameter (D_{BET}) rose from 2.9 nm to 6.4 nm. This characteristic is consistent with partial pore clogging by drug, which decreases accessible surface area and pore volume (Li et al., 2018). Upon functionalisation with TPP, a more complicated change in the NPs' structure was observed. The BET surface area dramatically decreased to 83.18 m^2/g and the micropore volume dropped to 0.004 cm^3/g. Notably, the DFT mode pore width increased significantly from 3.18 nm to 36.22 nm, indicating that the bulky TPP molecules might have disrupted the mesoporous structure. This interpretation is further supported by the increase in D_{BET} from 2.9 nm to 14.4 nm, suggesting a substantial decrease in the available surface area due to either the surface roughness or structural rearrangement. However, when OXA was loaded into this sample (Fe_3O_4@MSN-NH_2/TPP) a slight increase (from 0.004 cm^3/g to 0.009 cm^3/g) in micropore volume and a sharp drop in the DFT mode pore width (from 36.23 nm to 3.18 nm) were observed. It

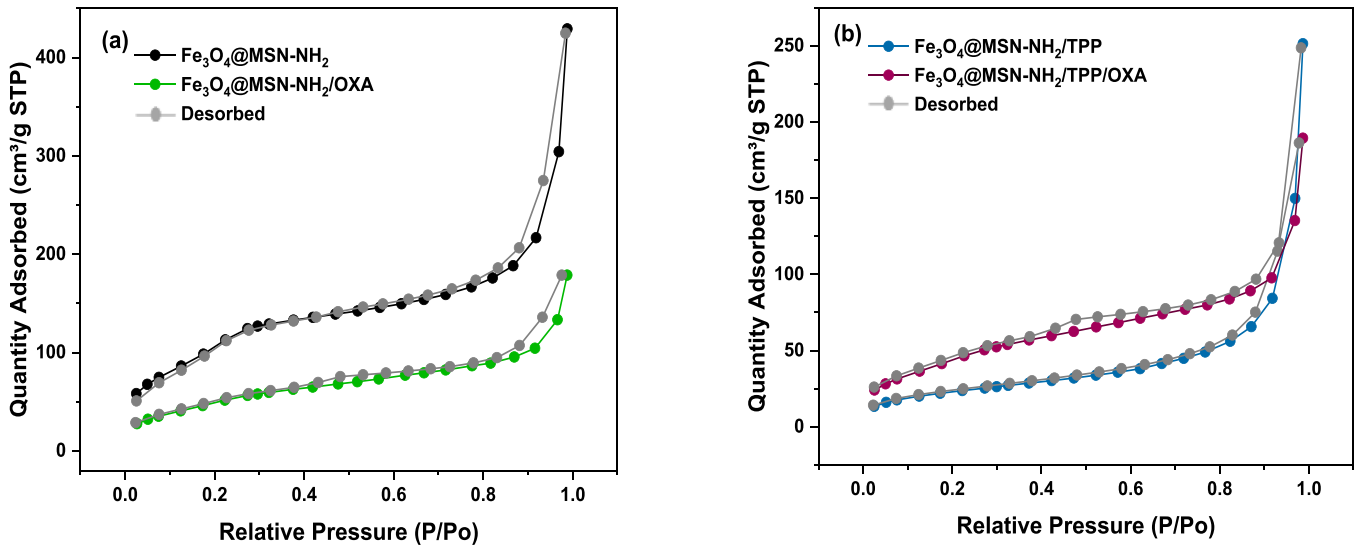

Fig. 6. Type IV N_2 adsorption-desorption isotherms for the BET surface area analyses of (a) Fe_3O_4@MSN-NH_2, Fe_3O_4@MSN-NH_2/OXA, (b) Fe_3O_4@MSN-NH_2/TPP and Fe_3O_4@MSN-NH_2/TPP/OXA.

Table 3
Summary of BET results of Fe_3O_4@MSN-NH_2, Fe_3O_4@MSN-NH_2/OXA, Fe_3O_4@MSN-NH_2/TPP and Fe_3O_4@MSN-NH_2/TPP/OXA.

Parameters	Fe_3O_4@MSN-NH_2	Fe_3O_4@MSN-NH_2/OXA	Fe_3O_4@MSN-NH_2/TPP	Fe_3O_4@MSN-NH_2/TPP/OXA
DFT Micropore Volume (cm^3/g)	0.086	0.019	0.004	0.009
DFT Mode (Pore Width) (nm)	3.18	3.06	36.22	3.18
DFT Pore Volume (cm^3/g)	0.569	0.257	0.324	0.259
BET S.A (m^2/g)	419.95	189.06	83.18	171.00
D_{BET} (nm)	2.9	6.4	14.4	7.0

BET particle diameter (D_{BET})

is evident that OXA loading might have caused the surface-conjugated TPP molecules to rearrange, leading to reopening some of the micro-pores for Fe_3O_4@MSN-NH_2/TPP/OXA. Additionally, the BET surface area expanded from 83.18 m^2/g to 171.00 m^2/g and the D_{BET} reduced from 14.4 nm to 7.0 nm, suggesting the surface become more accessible. These results highlight complex relationship between surface functionalisation and OXA loading. While loading OXA decreased porosity by occupying the pores, TPP conjugation resulted in structural modifications that alter pore architecture in a more complicated manner. However, the subsequent OXA loading seemed to reverse these changes, possibly by promoting molecular rearrangement and improved NPs' dispersion.

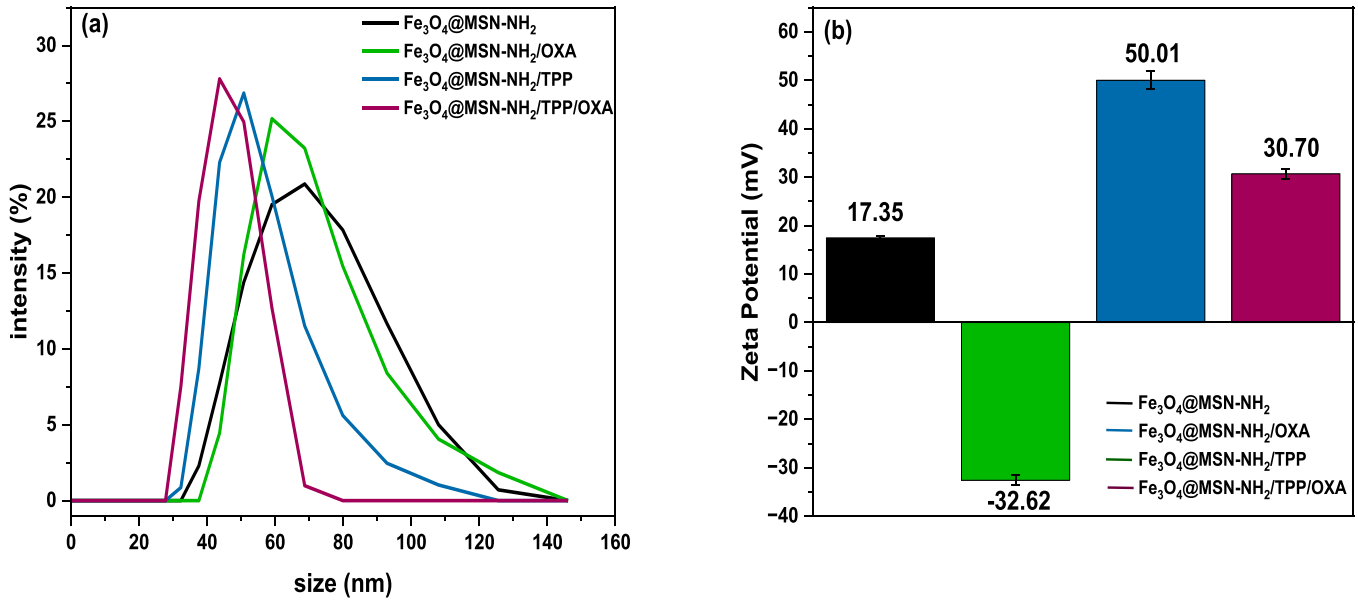

Fig. 7. **(a)** DLS measurements, D_H, and **(b)** Zeta potential measurement of Fe_3O_4@MSN-NH_2, Fe_3O_4@MSN-NH_2/TPP, Fe_3O_4@MSN-NH_2/OXA and Fe_3O_4@MSN-NH_2/TPP/OXA at 25 °C.

Fig. 7(a and b) shows the DLS and zeta potential measurements of Fe_3O_4@MSN-NH_2, Fe_3O_4@MSN-NH_2/OXA, Fe_3O_4@MSN-NH_2/TPP and Fe_3O_4@MSN-NH_2/TPP/OXA samples in HPLCW. The hydrodynamic size of Fe_3O_4@MSN-NH_2, Fe_3O_4@MSN-NH_2/OXA, Fe_3O_4@MSN-NH_2/TPP and Fe_3O_4@MSN-NH_2/TPP/OXA NPs were 68.7 nm, 59.1 nm, 50.8 nm, and 43.4 nm, respectively. When OXA was loaded, the hydrodynamic size of Fe_3O_4@MSN-NH_2 slightly reduced which suggested that the interaction between NH_2 groups may have stabilised the structure and increased the dispersibility. Additionally, the introduction of TPP onto the Fe_3O_4@MSN-NH_2 led to a further shrinkage in hydrodynamic size to 50.8 nm. The interaction of TPP, the lipophilic cation with the hydrophilic NH_2 groups might have influenced the configuration. Similarly, the OXA loaded sample showed, the size was reduced further to 43.4 nm, indicating both TPP and OXA interact simultaneously. The TPP might have improved the stability and the loading capacity of OXA and led to further reduction in hydrodynamic size.

The zeta potential value of Fe_3O_4@MSN-NH_2 was + 17.35 mV, due to the protonation of the NH_2 groups, which led to a moderately positive surface charge, suggesting the particles could be subject to aggregation. While loading OXA caused a significant drop in zeta potential value to −32.62 mV, revealed improved stability. The NH_2 groups typically generate positive charge under physiological conditions (e.g., water) following the protonation, while oxalate groups contribute to a negative surface charge. The negatively charged oxalate might have interacted with NH_2 groups of Fe_3O_4@MSN-NH_2, causing the overall surface charge to become negative. In addition, the conjugation of TPP onto the Fe_3O_4@MSN-NH_2 increased the zeta potential significantly (50.01 mV), and enhanced stability since it is a highly positive cation. Similarly, loading the OXA onto Fe_3O_4@MSN-NH_2/TPP decreased the surface charge to 30.70 mv. Although, OXA partially neutralised the highly positive TPP, the zeta potential value of 30.70 mV still demonstrated a good stability of the colloidal suspension, indicating a balance between OXA and TPP on the surface of NPs. Overall, there were correlation between the DLS hydrodynamic sizes and zeta potential values of the samples. As zeta potential approached more positive/negative values, it signified higher dispersion and lower aggregation, leading to a reduction in the hydrodynamic size (D_H) of the particles. The detailed D_H, zeta potential and polydispersity index (PDI) values, D_{BET} (nm), D_{TEM} (nm) and $D_{(311)}$ (nm), of the samples are collected in Table 4.

LUMiSizer was used to analysis the colloidal dispersion stability of Fe_3O_4@MSN-NH_2/OXA and Fe_3O_4@MSN-NH_2/TPP/OXA in PBS (pH 7.4) at different temperatures (4 °C, 25 °C, 37 °C, 43 °C). The multi-sample analyser utilises controlled centrifugal force to rapidly accelerate particle migration and phase separation in colloidal dispersions, allowing solely gravity-driven physical disruption such as sedimentation, creaming, flotation, and aggregation. It enables the measurement of velocity distribution in the centrifugal field through space and time resolved extinction profiles (STEP), offering details on the kinetics of the separation process, and particle migration. The analyser provides high-throughput stability testing and shelf-life estimation within a considerably reduced timescale (Mäkinen et al., 2015; Chiu et al., 2011; Xu et al., 2017b). Extinction profile have been applied to quantify instability processes, such as sedimentation and flotation velocity, rate of clarification, residual turbidity and the volume of segregated phases (liquid or solid) (Zielińska et al., 2019). The STEP profiles of Fe_3O_4@MSN-NH_2/TPP/OXA in PBS at 4 °C, 25 °C, 37 °C, 43 °C are provided in Fig. 8(a), where the light transmission intensity through the dispersed samples at different height of the cuvette over 50 min of centrifugation can be observed. At all tested temperatures the samples presented moderately stable colloidal dispersion, which could be due to the electrostatic repulsion induced by IONPs coating materials.

In addition to qualitative and kinetic measurements, the LUMiSizer allows dimensionless instability index, which is calculated by the SEPView® software. The parameter ranging from 0 (maximum stability) to 1 (minimum stability) used as an indicator for assessing the onset of phase separation based on clarification dynamics (Fernandes et al., 2017). The instability index values of Fe_3O_4@MSN-NH_2/OXA, and Fe_3O_4@MSN-NH_2/TPP/OXA are shown in Fig. 8(b). For all tested temperatures, the instability indices values remained below 1, reflecting stable dispersion. Notably, Fe_3O_4@MSN-NH_2/OXA performed worse at body temperature (37 °C) and slightly better at storage temperature (4 °C). While Fe_3O_4@MSN-NH_2/TPP/OXA sample demonstrated a better thermal stability at 43 °C, due to stabilising behaviour of TPP moiety, implying potential for thermo-responsive drug delivery induced by magnetic hyperthermia. In contrast, the system displayed low stability at 4 °C, likely attributable to decreased thermal energy and increased shell rigidity at low temperature.

In accordance with Lerche's space-time conversion principle (Lerche, 2002), accelerated centrifugation testing can be extrapolated to predict an estimated sedimentation period under standard gravitational conditions (g=9.81 m/s^2), reflecting stability and shelf-life of nano-formulations. The relative centrifugal force (RCF) was calculated based on formula below (Miron et al., 2019), where r is the radius of the instrument's rotor in cm (10 cm), and N is the rotational speed per minute (RPM).

$$RCF = 11.18.r.\left(\frac{N}{1000}\right)^2 \quad (5)$$

With an RCF of 1062.2 g, and a centrifugation duration of 50 min, the gravitational time was calculated as;

$$t_{gravity} = t_{centrifuge}\ \text{X RCF} \quad (6)$$

This modelling method estimated that both drug-loaded samples can maintain their colloidal dispersion stability for almost 37 days under normal gravitational conditions. However, it is essential to stress, the LUMiSizer instrument is not developed to model real-time chemical degradation (e.g., hydrolysis, oxidation), its temperature-controlled features are limited to simulating gravity-driven physical destabilisation across different temperature conditions.

Given the spherical to quasi-polyhedral morphology of the NPs obtained by TEM, calculating sedimentation velocity based on traditional Stokes' law might miscalculate hydrodynamic drag effects. To consider particle geometry, a shape-dependent correction factor (Φ) was incorporated as reported in literatures (Yang et al., 2021; Xie and Zhang, 2001; Laurenceau-Cornec et al., 2019; Ogolo et al., 2024), offering a more precise representation of settling profile of non-spherical particles. The modified Stokes' law is expressed as;

$$V_m = \frac{2r^2(\rho_p - \rho_f)g}{9\eta.\phi} \quad (7)$$

Table 4
D_H, ZP, and PDI results of NPs in water compared with the TEM and XRD resutls.

	Fe_3O_4@MSN-NH_2	Fe_3O_4@MSN-NH_2/OXA	Fe_3O_4@MSN-NH_2-TPP	Fe_3O_4@MSN-NH_2-TPP/OXA
D_H major mode (minor) (nm)	68.7 ± 8.3	59.1 ± 3.0	50.8 ± 6.4	43.7 ± 2.1
ZP major mode (minor) (mV)	+ 17.35 ± 2.04	−32.62 ± 1.91	+ 50.01 ± 1.01	+ 30.70 ± 1.18
PDI	0.116	0.101	0.107	0.104
D_{BET} (nm)	2.9	6.4	14.4	7.0
D_{TEM} (nm)	12.01 ± 0.5	12.57 ± 2	13.54 ± 1	14.26 ± 2
$D_{(311)}$ (nm)	8.58	7.55	8.00	9.30

Hydrodynamic size (D_H), Zeta potential (ZP), Polydispersity index (PDI)

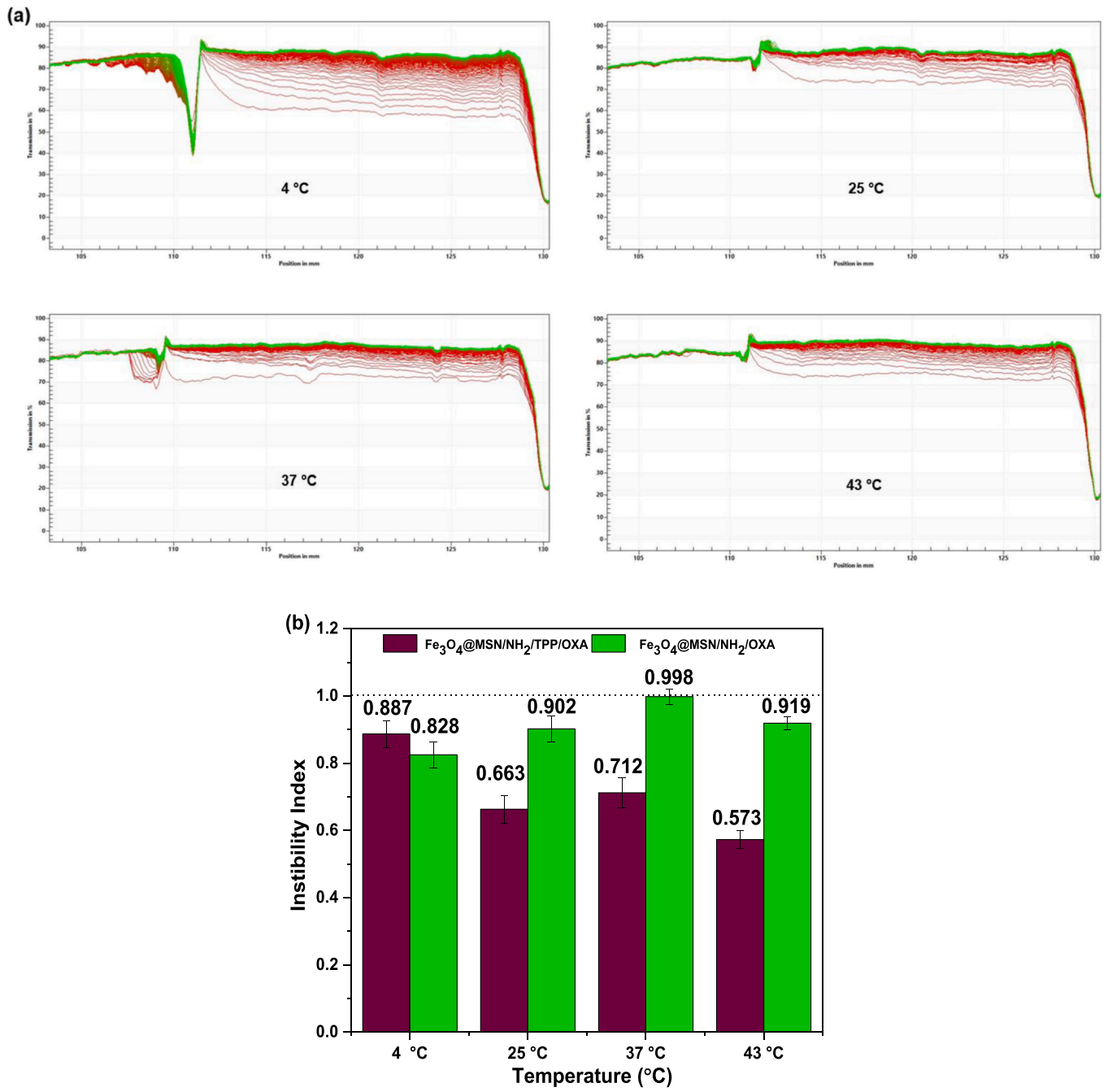

Fig. 8. (a) STEP profile of Fe_3O_4@MSN-NH_2/TPP/OXA and (b) Instability index of Fe_3O_4@MSN-NH_2/OXA and Fe_3O_4@MSN-NH_2/TPP/OXA at 4 °C, 25 °C, 37 °C and 43 °C at 3000 s and 3000 rpm.

V_m: Sedimentation velocity (m/s)
r: Hydrodynamic radius of the particle (m)
ρ_p: mass density of the particle (kg/m^3)
ρ_f: mass density of the fluid (kg/m^3)
g: acceleration due to gravity (9.81 m/s^2)
η: Dynamic viscosity of the fluid (Pa.s)
ϕ: dimensionless shape factor

With this adjustment, the estimated temperature specific shelf-lives across different temperatures were as follow; 128 days at 4 °C, 72 days at 25 °C, 56 days at 37 °C and 53 days at 43 °C. Together, the instability indices obtained from LUMiSizer with temperature-adjusted shelf-life estimation providing a multidimensional view of colloidal performance. It emphasises the necessity of incorporating both early-phase destabilisation and long-term sedimentation profiles to comprehensively assess the thermal resilience of NP-based therapeutic agent delivery system.

3.2. Drug loading and release

The drug loading capacity of OXA in Fe_3O_4@MSN-NH_2/OXA and Fe_3O_4@MSN-NH_2/TPP/OXA samples were determined by ICP-OE (pure OXA was used as reference). The samples (50 mg) were dissolved in aqua regia (10 ml) and heated for 2 h, then the solutions were made up to 50 ml by adding HPLCW. Then, 1 ml of samples was evaluated to detect the presence of platinum (Pt) element. Based on the molecular weight of Pt and the amount of initial sample, the concentration of Pt

was calculated.

The Pt loading capacity in OXA, Fe_3O_4@MSN-NH_2/OXA and Fe_3O_4@MSN-NH_2/TPP/OXA were 50.38 %, 5.07 % and 8.0 % respectively. Based on the molecular weight of OXA (i.e. 397.29 g/mol) the drug loading of Fe_3O_4@MSN-NH_2/OXA and Fe_3O_4@MSN-NH_2/TPP/OXA were 10.33 % and 16.29 %, respectively. It is worth noting that these values are significantly lower than the previously reported OXA loaded capacity for Fe_3O_4@MSN-NH_2 (Tabasi et al., 2021). This might be due to the fact than in our study, OXA has been mostly loaded on the surface of NPs. Assuming the occupied surface on the nanoparticles is controlled by the size of OXA molecule (ca 0.9 nm), one could geometrically estimate the maximum theoretical surface loading capacity for the NPs. For the full mono-layer surface coverage of Fe_3O_4@MSN-NH_2 and Fe_3O_4@MSN-NH_2/TPP particles with roughly 12.01 and 13.54 nm in sizes (from TEM, Table 4), about 712 and 905 molecules of OXA are required, respectively. These constitute maximum mass loadings (theoretical) capacities of about 10.0 % and 8.9 % for mono-layer surface coverage in the cases of Fe_3O_4@MSN-NH_2/OXA and Fe_3O_4@MSN-NH_2/TPP/OXA, respectively. By comparing these values with the measured drug loading of Fe_3O_4@MSN-NH_2/OXA and Fe_3O_4@MSN-NH_2/TPP/OXA, it can be postulated that in this work, the NPs are sufficiently covered by the drug molecules.

Drug release study was performed on pure Fe_3O_4@MSN-NH_2/OXA and Fe_3O_4@MSN-NH_2/TPP/OXA at pH 7.4 (normal body pH) and pH 5 (cancer cell line) conditions. As shown in Fig. 9, Fe_3O_4@MSN-NH_2/OXA, Fe_3O_4@MSN-NH_2/TPP/OXA samples had a minimal release (~<10 %) in PBS (pH 7.4) over 48 h. The samples remained stable in neutral pH conditions, suggesting minimal premature release in blood-like circulation prior to reach their target site at tumour microenvironment (TME). While under acidic conditions (in acetate buffer (AcB)) both samples exhibited considerably high release profile, Fe_3O_4@MSN-NH_2/OXA in AcB started with a moderate release after 3 h to 30.66 %, then slightly increased to 38.15 % after 6 h and continued to steadily increase over time (after 9 h 45 % release). The significantly high release rate in acidic condition (pH 5) could be due to the presence of NH_2 groups that were protonated.

At 12 h, Fe_3O_4@MSN-NH_2/TPP/OXA released ~ 80 % of its OXA cargo, while Fe_3O_4@MSN-NH_2/OXA released about 60 %. This significant difference suggests that TPP conjugation accelerated rate of release of OXA in acidic conditions. After the rapid release profile, the Fe_3O_4@MSN-NH_2/TPP/OXA reached a plateau (~90 %). The fast initial release followed by sustained release over time could be advantageous in preventing the rapid cancer cell growth and leading to apoptosis. Table 5. Provide accumulative release data for Fe_3O_4@MSN-NH_2/OXA and Fe_3O_4@MSN-NH_2TPP/OXA in AcB and PBS, pH 5 and pH 7.4, respectively for 48 h. It should be noted that although the results are promising, future studies should also focus on *in vitro* release of drug in an environment closer to the biological systems.

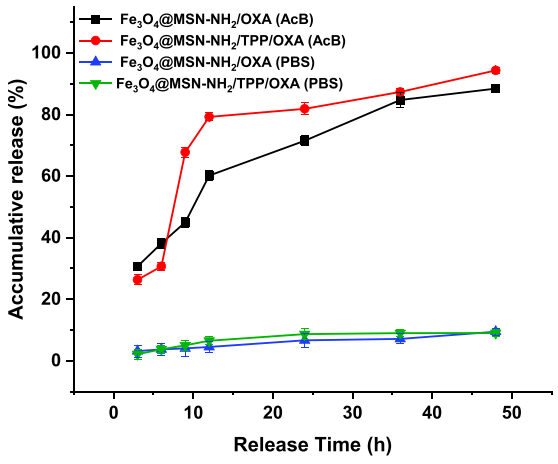

Fig. 9. Drug release test by HPLC-UV in 48 h for Fe_3O_4@MSN-NH_2/OXA and Fe_3O_4@MSN-NH_2TPP/OXA in AcB.

Table 5
Accumulative release profile of Fe_3O_4@MSN-NH_2/OXA and Fe_3O_4@MSN-NH_2TPP/OXA in AcB and PBS, pH 5 and pH 7.4, respectively for 48 h.

Time (h)	Accumulative Release (%) in AcB		Accumulative Release (%) in PBS	
	Fe_3O_4@MSN-NH_2/OXA	Fe_3O_4@MSN-NH_2TPP/OXA	Fe_3O_4@MSN-NH_2/OXA	Fe_3O_4@MSN-NH_2TPP/OXA
3	30.66	26.31	3.16	3.16
6	38.15	30.66	3.71	3.71
9	45.00	67.74	5.03	5.03
12	60.17	79.23	4.50	6.50
24	71.49	81.86	6.67	8.68
36	84.76	87.34	7.12	8.99
48	88.43	94.33	9.34	9.03

3.3. Magnetic properties

The Magnetic hysteresis curves of Fe_3O_4@MSN-NH_2, Fe_3O_4@MSN-NH_2/TPP, Fe_3O_4@MSN-NH_2/OXA and Fe_3O_4@MSN-NH_2/TPP/OXA NPs at 300 K showed superparamagnetic behaviour (Fig. 10 (a and b)). The saturation magnetisation (M_s) of Fe_3O_4@MSN-NH_2 sample was 61.24 emu/g, which was considerably higher than other reported data, i.e. 25 emu/g (Tabasi et al., 2022), 28.5 emu/g (Li et al., 2014), and 41 emu/g (Fang et al., 2019) (please see Table 6). Once OXA was loaded onto Fe_3O_4@MSN-NH_2 sample the M_s slightly reduced to 55.35 emu/g, while modification of Fe_3O_4@MSN-NH_2 by TPP, resulted the magnetic response to decrease further to 42.09 emu/g. Following the loading of OXA onto Fe_3O_4@MSN-NH_2/TPP, the M_s had a minor increase to 43.42 emu/g. The results of other magnetic properties are collected in Table 7. All in all, the drug loaded NPs show good magnetic behaviour in response to an EXMF (please see the videos in SI2).

3.4. In vitro cytotoxicity

The growth inhibition of CT26 cells treated with Fe_3O_4@MSN-NH_2, Fe_3O_4@MSN-NH_2/TPP, Fe_3O_4@MSN-NH_2/OXA, Fe_3O_4@MSN-NH_2/TPP/OXA and pure OXA drug with 50 μg/ml concentration is shown in Fig. 11. As expected, growth inhibition of CT26 was observed with pure OXA. By contrast, unloaded Fe_3O_4@MSN-NH_2 and Fe_3O_4@MSN-NH_2/TPP nanoparticles' ability to inhibit CT26 cells growth was limited even at highest dose tested (50 μg/ml), indicating these particles are comparatively non cytotoxic to CT26 mouse cancer cells. Importantly, a dose-dependent decrease in cell growth compared to control was observed in Fe_3O_4@MSN-NH_2/OXA after 96 h exposure. A dose dependent growth inhibition of CT26 was also observed with the Fe_3O_4@MSN-NH_2/TPP/OXA particles, but there was no statistically significant difference in growth inhibition between Fe_3O_4@MSN-NH_2/OXA, and Fe_3O_4@MSN-NH_2/TPP/OXA (2-way ANOVA, $p > 0.05$). The IC50 values, i.e. the concentration at which 50 % of cell growth is inhibited, for pure OXA, Fe_3O_4@MSN-NH_2/OXA, and Fe_3O_4@MSN-NH_2/TPP/OXA following 96 h exposure in CT26 cells were 2.0 ± 0.8, 6.7 ± 0.4 and 11.0 ± 2.0 μg/ml respectively. Based on the actual drug loading of NPs, as reported in Section 3.2, the IC50 values calculated based on the corresponding free OXA concentration would be 0.69 ± 0.041 and 1.80 ± 0.33 μg/ml for Fe_3O_4@MSN-NH_2/OXA, and Fe_3O_4@MSN-NH_2/TPP/OXA NPs, respectively. All the data are provided in Table 8. It can be seen that the IC50 value for Fe_3O_4@MSN-NH_2/OXA is significantly lower than the IC50 of pure OXA (2.0 ± 0.8) which suggests an improved drug delivery to the cells when OXA is loaded onto the NPs. It is worth noting that Fe_3O_4@MSN-NH_2/TPP/OXA had a higher IC50 value than Fe_3O_4@MSN-NH_2/OXA.

Although Fe_3O_4@MSN-NH_2/TPP/OXA did not impose higher cytotoxicity in comparison to Fe_3O_4@MSN-NH_2/OXA in CT26 cells, the conjugation of TPP facilitates notable therapeutic advantages, i.e.

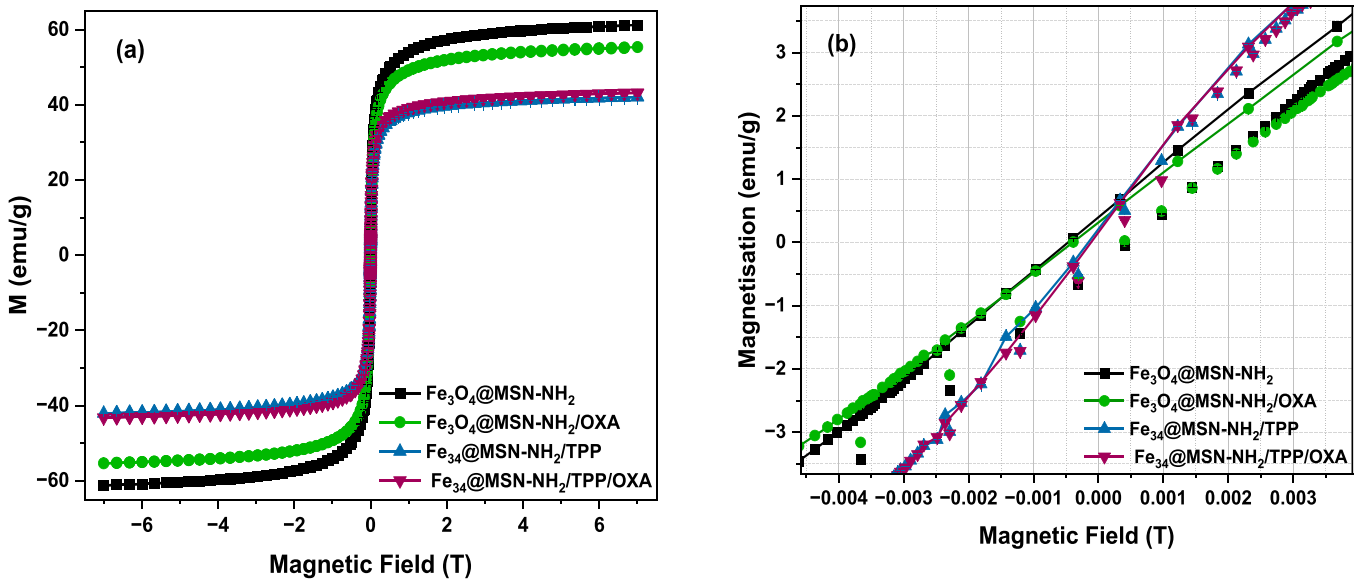

Fig. 10. (a and b). Magnetisation hysteresis loop of the Fe_3O_4@MSN-NH_2, Fe_3O_4@MSN-NH_2/TPP, Fe_3O_4@MSN-NH_2/OXA and Fe_3O_4@MSN-NH_2/TPP/OXA NPs at 300 K.

Table 6
Comparison of saturation magnetisation of Fe_3O_4@MSN-NH_2 with the literatures.

Samples	Fe_3O_4@MSN-NH_2 Our Study	Fe_3O_4@MSN-NH_2 Tabasi et al., (2022)	Fe_3O_4@MSN-NH_2 Li et al., (2014)	Fe_3O_4@MSN-NH_2 Fang et al., (2019)
M_s (emu/g)	61.24	25.00	28.50	41.00
D_{TEM} (nm)	12	14.0	9.0	90.0–110.0

M_s: Saturation magnetisation
D_{TEM} (nm): Mean diameter of primary particles by TEM

Table 7
Magnetic properties of the Fe_3O_4@MSN-NH_2, Fe_3O_4@MSN-NH_2/TPP, Fe_3O_4@MSN-NH_2/OXA and Fe_3O_4@MSN-NH_2/TPP/OXA NPs at 300 K.

Samples	Fe_3O_4@MSN-NH_2	Fe_3O_4@MSN-NH_2/OXA	Fe_3O_4@MSN-NH_2/TPP	Fe_3O_4@MSN-NH_2/TPP/OXA
H_c (T)	0.00048(2)	0.00038(2)	0.00055(2)	0.00014(2)
M_r (emu/g)	0.398	0.303	0.073	0.192
M_s (emu/g)	61.24	55.35	42.09	43.42
M_r/M_s	0.0065	0.00571	0.0017	0.0044
D_{TEM} (nm)	1201 ± 0.5	12.57 ± 2	13.54 ± 1	14.26 ± 2
$D_{(311)}$ by XRD (nm)	8.58	7.55	8.00	9.30

M_r: Remnant magnetisation (The residual magnetisation in Fe_3O_4 NPs when XMF is removed.
H_c: Coercive Field (the strength of the utilized magnetic field needed to reduce the magnetization of Fe_3O_4 NPs to zero).
M_s: The highest magnetisation (saturation magnetisation).
M_r/M_s: Remnant magnetisation (emu/g)/Saturation magnetisation (emu/g) is normalised remnant magnetisation; the value of this ratio shows the residual magnetisation in materials after saturation.
($D_{(311)}$) by XRD: Crystallite size.
D_{TEM} (nm): Mean diameter of primary particles by TEM.

mitochondrial targeting. The TPP modification was aimed at providing mitochondrial targeting and immunogenic cell death, which will be explored in future *in vitro/in vivo* studies. In addition, the stability of NPs in cell culture medium will be fully investigated in future extended studies to fully study their long-term therapeutic performance.

4. Conclusion

In this study, OXA drug loaded, TPP-functionalised Fe_3O_4@MSN-NH_2 nanoparticles were successfully developed for targeted cancer treatment. XPS and FT-IR analyses demonstrated successful TPP conjugation and OXA loading, while VMS analysis demonstrated good magnetic properties of NPs upon functionalisation and drug loading. ICP-OES quantified a drug loading (wt%) of 10.33 % and 16.29 % in Fe_3O_4@MSN-NH_2/OXA and Fe_3O_4@MSN-NH_2/TPP/OXA, respectively. Notably, drug release studies demonstrated that the TPP-functionalised system exhibited rapid and enhanced drug release under acidic conditions (pH 5), achieving over 80 % release within 10 h, suggesting its suitability for tumor microenvironments. *In vitro* cytotoxicity tests on CT26 colon cancer cells revealed that corresponding OXA concentration delivered by Fe_3O_4@MSN- Fe_3O_4@MSN-NH_2/OXA and NH_2/TPP/OXA (IC_{50}= 0.69 ± 0.041 and 1.80 ± 0.33 μg/ml, respectively) is lower than the free OXA (IC_{50}= 2.0 ± 0.8) likely due to the effective drug release facilitated by NPs. This study could be limited to *in vitro* experiments, which do not fully reflect the NPs' behaviour in physiological conditions. Our future work should include (i) *In vivo* evaluations to study biodistribution, pharmacokinetics, and efficacy, (ii) Stability testing to ensure robustness under physiological conditions, (iii) Optimisation of TPP functionalisation to balance controlled release and reduce drug resistance, and (iv) Combinatorial therapies with other drugs or targeting ligands to enhance treatment efficacy. Addressing these limitations will assist advance our Fe_3O_4@MSN-NH_2/TPP/OXA system toward clinical applications.

Declaration of Competing Interest

The authors declare that they have no known competing financial interests or personal relationships that could have appeared to influence the work reported in this paper.

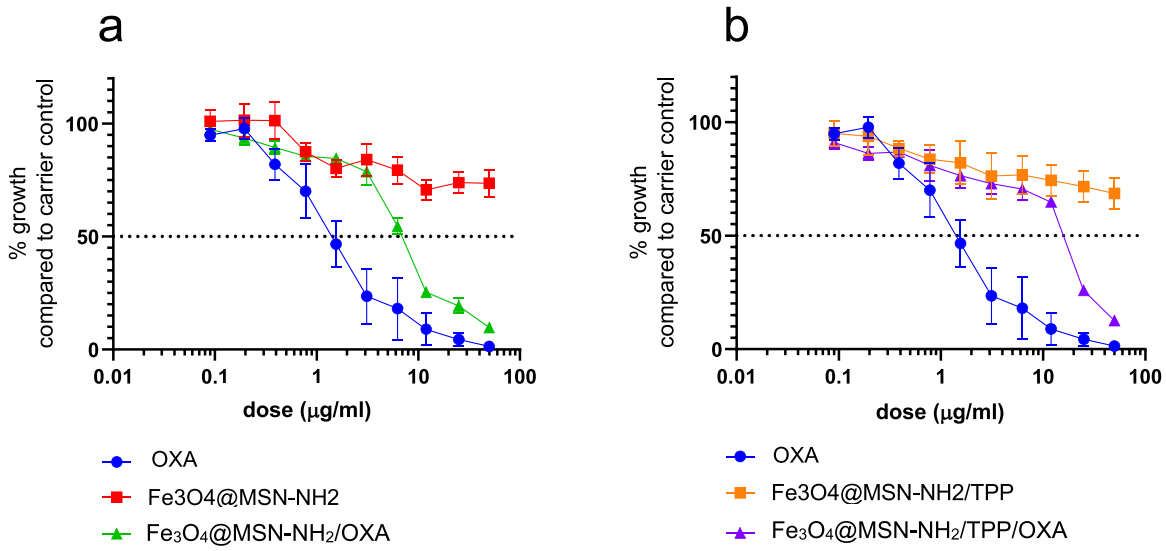

Fig. 11. Dose response curve for free OXA, Fe_3O_4@MSN-NH_2 and Fe_3O_4@MSN-NH_2/OXA (a), and free OXA, Fe_3O_4@MSN-NH_2/TPP and Fe_3O_4@MSN-NH_2/TPP/OXA (b) in CT26 mouse colorectal cancer cells after 96 h exposure. Growth inhibition was determined using the MTT assay. Data represent the percentage growth inhibition compared to carrier control treated cells and are expressed as mean percentage + /- standard error of the mean for 3 independent replicates.

Table 8
IC_{50} values for Fe_3O_4@MSN-NH_2, Fe_3O_4@MSN-NH_2/TPP, Fe_3O_4@MSN-NH_2/OXA and Fe_3O_4@MSN-NH_2/TPP/OXA NPs on CT26 cells.

Samples	Mean IC50 + /- SEM (µg/ml) following 96 h exposure	Mean IC50 + /- SEM (µg/ml) following 96 h exposure – corresponding OXA concentration delivered
OXA	2.0 ± 0.8	2.0 ± 0.8
Fe_3O_4@MSN-NH_2	No difference	No difference
Fe_3O_4@MSN-NH_2/OXA	6.7 + /−0.4	0.69 ± 0.041
Fe_3O_4@MSN-NH_2/TPP	No difference	No difference
Fe_3O_4@MSN-NH_2/TPP/OXA	11.0 ± 2.0	1.80 ± 0.33

Acknowledgement

Masome Moeni would like to acknowledge the University of Leeds for the Sanctuary Scholarship and Mr Alex Ferguson for his guidance and assistance. The authors would like to thank the technical support, training and access to analytical equipment provided by Dr. Ben Douglas, Dr Adrian Cunliffe and Mr Simon Lloyd (School of Chemical and Process Engineering, University of Leeds), Dr Zabeada Islam (Leeds electron microscopy and spectroscopy centre), Dr Christopher Pask and Dr Jeanine Williams (School of Chemistry, University of Leeds) and Mr Robert Haris for providing technical support, Ailsa Rosa, Hanyang Sun, and Ewa Jaworska (Leeds Institute of Medical Research, St James Hospital).

Appendix A. Supporting information

Supplementary data associated with this article can be found in the online version at doi:10.1016/j.cherd.2025.06.042.

References

Yang, Y., Huang, M., Qian, J., Gao, D., Liang, X., 2020. Tunable Fe3O4 nanorods for enhanced magnetic hyperthermia performance. Sci. Rep. 10.
Sabzi dizajyekan, B., Jafari, A., Vafaie-Sefti, M., Saber, R., Fakhroueian, Z., 2024. Preparation of stable colloidal dispersion of surface modified Fe3O4 nanoparticles for magnetic heating applications. Sci. Rep. 14.
Aram, E., Moeni, M., Abedizadeh, R., Sabour, D., Sadeghi-Abandansari, H., Gardy, J., Hassanpour, A.J.N., 2022. Smart and multi-functional magnetic nanoparticles for cancer treatment applications: clinical challenges and future prospects, 12.
Liu, S., Yu, B., Wang, S., Shen, Y., Cong, H., 2020. Preparation, surface functionalization and application of Fe3O4 magnetic nanoparticles. Adv. Colloid Interface Sci. 281, 102165.
Shen, L., Li, B., Qiao, Y., 2018. Fe3O4 nanoparticles in targeted drug/gene delivery systems. Materials 11.
Palma, F.R., Gantner, B.N., Sakiyama, M.J., Kayzuka, C., Shukla, S., Lacchini, R., Cunniff, B., Bonini, M.G., 2023. ROS production by mitochondria: function or dysfunction? Oncogene.
Dong, H., Du, W., Dong, J.-l, Che, R., Kong, F., Cheng, W., Ma, M., Gu, N., Zhang, Y., 2022. Depletable peroxidase-like activity of Fe3O4 nanozymes accompanied with separate migration of electrons and iron ions. Nat. ommun. 13.
Moeni, M., Edokali, M., Rogers, M., Cespedes, O., Tliba, L., Habib, T., Menzel, R., Hassanpour, A., 2024. Effect of reaction and post-treatment conditions on physico-chemical properties of magnetic iron oxide nano-particles. Particuology.
Aram, E., Sadeghi-Abandansari, H., Radmanesh, F., Khorasani, H.R., Nowroozi, M.R., Hassanpour, A., Baharvand, H., Sabour, D., 2024. Shell-sheddable and charge switchable magnetic nanoparticle as pH-sensitive nanocarrier for targeted drug delivery applications. Polym. Adv. Technol.
Jeshvaghani, P.A., Pourmadadi, M., Yazdian, F., Rashedi, H., Khoshmaram, K., Nigjeh, M.N., 2022. Synthesis and characterization of a novel, pH-responsive sustained release nanocarrier using polyethylene glycol, graphene oxide, and natural silk fibroin protein by a green nano emulsification method to enhance cancer treatment. Int. J. Biol. Macromol.
Li, J., Wang, Y., Yu, X., 2021. Magnetic molecularly imprinted polymers: synthesis and applications in the selective extraction of antibiotics. Front. Chem. 9.
Yu, C., Wang, Z., Sun, Z., Zhang, L., Zhang, W., Xu, Y., Zhang, J.J., 2020. Platinum-based combination therapy: molecular rationale, current clinical uses, and future perspectives. J. Med. Chem.
Wu, Y., Liang, Y., Liu, Y.D., Hao, Y., Tao, N., Li, J., Sun, X., Zhou, M., Liu, Y.J., 2021. A Bi2S3-embedded gellan gum hydrogel for localized tumor photothermal/antiangiogenic therapy. J. Mater. Chem. 9 (14), 3224–3234.
Zafar, H., F. Raza, S. Ma, Y. Wei, J. Zhang and Q.J.Bs Shen, Recent Progress on Nanomedicine-induced Ferroptosis for Cancer Therapy. 2021.
Alcindor, T., Beauger, N., 2011. Oxaliplatin: a review in the era of molecularly targeted therapy. Curr. Oncol. 18 (1), 18–25.
Yothers, G., O'connell, M.J., Allegra, C.J., Kuebler, J.P., Colangelo, L.H., Petrelli, N.J., Wolmark, N., 2011. Oxaliplatin as adjuvant therapy for colon cancer: updated results of NSABP C-07 trial, including survival and subset analyses. J. Clin. Oncol. Off. J. Am. Soc. Clin. Oncol. 29 (28), 3768–3774.
Zhang, C., Xu, C., Gao, X., Yao, Q., 2022. Platinum-based drugs for cancer therapy and anti-tumor strategies. Theranostics 12, 2115–2132.
Liu, D., Li, X.-w, Chen, C., Li, C., Zhou, C.-b, Zhang, W., Zhao, J.-g, Fan, J., Cheng, K., Chen, L., 2018. Target-specific delivery of oxaliplatin to HER2-positive gastric cancer cells in vivo using oxaliplatin-au-fe3o4-herceptin nanoparticles. Oncol. Lett. 15 5, 8079–8087.

Kohan Hoosh Nejad, A., Ahmad panahi, H., Keshmirizadeh, E., Torabi Fard, N., 2023. Fabrication of a pH-responsive drug delivery system based on the super-paramagnetic metal-organic framework for targeted delivery of oxaliplatin. Int. J. Polym. Mater. Polym. Biomater. 72, 1083–1092.
Wu, F., Du, Y., Yang, J., Shao, B., Mi, Z., Yao, Y., Cui, Y., He, F., Zhang, Y., Yang, P., 2022. Peroxidase-like active nanomedicine with dual glutathione depletion property to restore oxaliplatin chemosensitivity and promote programmed cell death. ACS nano.
Chen, Q., Liu, L., Lu, Y., Chen, X., Zhang, Y., Zhou, W., Guo, Q., Li, C., Zhang, Y., Zhang, Y., Liang, D., Sun, T., Jiang, C., 2019. Tumor microenvironment-triggered aggregated magnetic nanoparticles for reinforced image-guided immunogenic chemotherapy. Adv. Sci. 6.
Tabasi, H., Mosavian, M.T.H., Sabouri, Z., Khazaei, M., Darroudi, M.J.I.C.C., 2021. pH-responsive and CD44-targeting by Fe3O4/MSNs-NH2 nanocarriers for Oxaliplatin loading and. Colon Cancer Treat. 125, 108430.
Prasun, P., 2019. Mitochondria and cancer. Mitochondrial Med.
Liberman, E.A., Topaly, V.P., Tsofina, L.M., Iasaïtis, A.A., Skulachev, V.P., 1969. Ion transport and electrical potential of mitochondrial membranes. Biokhimiia 34 (5), 1083–1087.
Smith, R.A.J., Hartley, R.C., Murphy, M.P., 2011. Mitochondria-targeted small molecule therapeutics and probes. Antioxid. Redox Signal. 15 (12), 3021–3038.
Xu, Y., Wang, S., Chan, H.F., Liu, Y., Li, H., He, C., Li, Z., Chen, M., 2017a. Triphenylphosphonium-modified poly(ethylene glycol)-poly(ε-caprolactone) micelles for mitochondria- targeted gambogic acid delivery. Int. J. Pharm. 522 (1-2), 21–33.
Sivagnanam, S., Das, K., Pan, I., Stewart, A., Barik, A., Maity, B., Das, P., 2023. Engineered triphenylphosphonium-based, mitochondrial-targeted liposomal drug delivery system facilitates cancer cell killing actions of chemotherapeutics. RSC Chem. Biol. 5, 236–248.
Jiang, L., Zhou, S., Zhang, X., Li, C., Ji, S., Mao, H., Jiang, X., 2021. Mitochondrion-specific dendritic lipopeptide liposomes for targeted sub-cellular delivery. Nat. Commun. 12.
Vinita, N.M., Devan, U., Durgadevi, S., Anitha, S., Prabhu, D., Rajamanikandan, S., Govarthanan, M., Yuvaraj, A., Biruntha, M., Antony Joseph Velanganni, A., Jeyakanthan, J., Prakash, P.A., Mohamed Jaabir, M.S., Kumar, P., 2023. Triphenylphosphonium conjugated gold nanotriangles impact Pi3K/AKT pathway in breast cancer cells: a photodynamic therapy approach. Sci. Rep. 13.
Hu, T., Gong, X., Liu, X., Xu, H., Zhou, F., Tan, S., He, Y., 2023. Smart design of a therapeutic nanoplatform for mitochondria-targeted copper-depletion therapy combined with chemotherapy. J. Mater. Chem. B.
Sun, K., Gao, Z., Zhang, Y., Wu, H., You, C., Wang, S., An, P., Sun, C., Sun, B., 2018. Enhanced highly toxic reactive oxygen species levels from iron oxide core-shell mesoporous silica nanocarrier-mediated Fenton reactions for cancer therapy. J. Mater. Chem. B (6 37), 5876–5887.
Kaneko, M., Yamazaki, H., Ono, T., Horie, M., Ito, A., 2023. Effective magnetic hyperthermia induced by mitochondria-targeted nanoparticles modified with triphenylphosphonium-containing phospholipid polymers. Cancer Sci. 114, 3750–3758.
Grisolia, A., De Santo, M., Curcio, M., Cavallaro, P.A., Morelli, C., Leggio, A., Pasqua, L., 2024. Engineered Mesoporous silica-based nanoparticles: characterization of surface properties. Materials 17.
Mudhakir, D., Sadaqa, E., Permana, Z., Mumtazah, J.E., Zefrina, N.F., Xeliem, J.N., Hanum, L.F., Kurniati, N.F., 2024. Dual-functionalized mesoporous silica nanoparticles for celecoxib delivery: amine grafting and imidazolyl PEI gatekeepers for enhanced loading and controlled release with reduced toxicity. Molecules 29.
Estevão, B.M., Miletto, I., Hioka, N., Marchese, L., Gianotti, E., 2021. Mesoporous silica nanoparticles functionalized with amino groups for biomedical applications. ChemistryOpen 10, 1251–1259.
Petreanu, I., Niculescu, V.C., Enache, S., Iacob, C., Teodorescu, M., 2022. Structural CHaracterization of Silica and Amino-silica Nanoparticles by Fourier Transform Infrared (FTIR) and Raman Spectroscopy. Anal. Lett. 56, 390–403.
Beamson, G., Briggs, D.R., 1992. High Resolution XPS of Organic Polymers: The Scienta ESCA300 Database.
Henderson, J.D., Payne, B.P., McIntyre, N.S., Biesinger, M.C., 2025. Enhancing oxygen spectra interpretation by calculating oxygen linked to adventitious carbon. Surf. Interface Anal. 57.
Yakushi, K., Yamakado, H., Ida, T., Ugawa, A., 1991. d-π interaction in conducting phthalocyaninatocobalt hexafluoroarsenate, CoPc(AsF6)0.5. Solid State Commun. 78, 919–923.
Stewart, S., Maloney, R., Sun, Y., 2023. Triphenylphosphine oxide promoting visible-light-driven C-C coupling via desulfurization. Chem. Commun.
Wind, J., Villeneuve, P., Taty, M.P.E., Figueroa-Espinoza, M.-C., Baréa, B., Pradelles, R., Durand, E., 2024. Improving the triphenylphosphine/triphenylphosphine oxide (TPP/TPPO)-based method for the absolute and accurate quantification by FTIR-ATR of hydroperoxides in oils or lipid extracts. Eur. J. Lipid Sci. Technol.
Sharma, P., Yadav, S.J., Shah, D.V., 2024. Synthesis, characterizations, and applications of Fe3O4 and Co-doped Fe3O4 nanomaterials. Braz. J. Phys.
Radoń, A., Drygała, A., Hawełek, Ł., Łukowiec, D., 2017. Structure and optical properties of Fe3O4 nanoparticles synthesized by co-precipitation method with different organic modifiers. Mater. Charact. 131, 148–156.
Khalid, A., Ahmed, R.M., Taha, M., Soliman, T.S., 2023. Fe3O4 nanoparticles and Fe3O4@SiO2 core-shell: synthesize, structural, morphological, linear, and nonlinear optical properties. J. Alloy. Compd.
Divya, S., Lims, S.C., Manivannan, M., Robert, R., Jerome Das, S., José, M., 2022. Impact of amorphous SiO2 as shell material on superparamagnetic Fe3O4 nanoparticles and investigation of temperature and frequency dependent dielectric properties. J. Alloy. Compd.
Cullity, B.D., Stock, S.R., 2001. Elements of X-ray Diffraction, Third ed.
Sánchez-Bajo, F., Ortiz, A.L., Cumbrera, F.L., 2008. An analytical model for the determination of crystallite size and crystal lattice microstrain distributions in nanocrystalline materials from the variance of the X-ray diffraction peaks. Appl. Phys. A 94, 189–194.
Ambrož, F., Macdonald, T.J., Martis, V., Parkin, I.P., 2018. Evaluation of the BET theory for the characterization of meso and microporous MOFs. Small Methods.
Shields, L.S., Thomas, J.E., Thommes, M.A., Thomas, hJ.E., Ma, M.A.T., 2006. Characterization of Porous Solids and Powders: Surface Area, Pore Size and Density.
Li, J., Shen, S., Kong, F., Jiang, T., Tang, C., Yin, C., 2018. Effects of pore size on in vitro and in vivo anticancer efficacies of mesoporous silica nanoparticles. RSC Adv. 8, 24633–24640.
Mäkinen, O.E., Uniacke-Lowe, T., O'Mahony, J.A., Arendt, E.K., 2015. Physicochemical and acid gelation properties of commercial UHT-treated plant-based milk substitutes and lactose free bovine milk. Food Chem. 168, 630–638.
Chiu, H.T., Chang, C.-Y., Chiang, T.-Y., Kuo, M.T., Wang, Y.-h, 2011. Using analytical centrifugation to characterize the dispersibility and particle size distributions of organic/inorganic composite coatings. J. Polym. Res. 18, 1587–1596.
Xu, D., Qi, Y., Wang, X., Li, X., Wang, S., Cao, Y., Wang, C., Sun, B., Decker, E.A., Panya, A., 2017b. The influence of flaxseed gum on the microrheological properties and physicochemical stability of whey protein stabilized β-carotene emulsions. Food Funct. 8 (1), 415–423.
Zielińska, A., Ferreira, N.R., Durazzo, A., Lucarini, M., Cicero, N., Mamouni, S.E., Silva, A.M., Nowak, I., Santini, A., Souto, E.B., 2019. Development and optimization of alpha-pinene-loaded solid lipid nanoparticles (SLN) using experimental factorial design and dispersion analysis. Molecules 24.
Fernandes, A.R., Ferreira, N.R., Fangueiro, J.F., Santos, A.C., Veiga, F., Cabral, C., Silva, A.M., Souto, E.B., 2017. Ibuprofen nanocrystals developed by 22 factorial design experiment: a new approach for poorly water-soluble drugs. In: Saudi Pharmaceutical Journal: SPJ, 25, pp. 1117–1124.
Lerche, D.P.D., 2002. Dispersion stability and particle characterization by sedimentation kinetics in a centrifugal field. J. Dispers. Sci. Technol. 23, 699–709.
Miron, R.J., Pinto, N.R., Quirynen, M., Ghanaati, S., 2019. Standardization of relative centrifugal forces in studies related to platelet-rich fibrin. J. Periodontol.
Yang, F., Zeng, Y., Huai, W., 2021. A new model for settling velocity of non-spherical particles. Environ. Sci. Pollut. Res. 28, 61636–61646.
Xie, H.-Y., Zhang, D., 2001. Stokes shape factor and its application in the measurement of sphericity of non-spherical particles. Powder Technol. 114, 102–105.
Laurenceau-Cornec, E.C., Le Moigne, F.A.C., Gallinari, M., Moriceau, B., Toullec, J., Iversen, M.H., Engel, A., De La Rocha, C.L., 2019. New guidelines for the application of Stokes' models to the sinking velocity of marine aggregates. Limnol. Oceanogr. 65.
Ogolo, N.A., Onyekonwu, M.O., Michael, A.T., 2024. Problems of Stokes' law application in determining the settling velocity of clays. J. Eng. Sci. Innov.
Tabasi, H., Mosavian, M.T.H., Darroudi, M., Khazaei, M., Hashemzadeh, A., Sabouri, Z., 2022. Synthesis characterization aminefunctionalized Fe3O4/Mesoporous Silica Nanoparticles (MSNs) potential nanocarriers drug delivery systems. J. Porous Mater. 29, 1817–1828.
Li, P.-X., Yu, Y., Liu, H., Cao, C., Song, W., 2014. A core-shell-satellite structured Fe3O4@MS-NH2@Pd nanocomposite: a magnetically recyclable multifunctional catalyst for one-pot multistep cascade reaction sequences. Nanoscale 6 (1), 442–448.
Fang, Z., Li, X., Xu, Z., Du, F., Wang, W., Shi, R., Gao, D.J.I.Jo.N., 2019. Hyaluronic acid-modified mesoporous silica-coated superparamagnetic Fe3O4 nanoparticles for targeted drug delivery. Int. J. Nanomed. 14, 5785–5797.